

1 **Title: Multi-organ functions of yolk sac during human early development**

2

3 **Authors:** Rachel A Botting^{1†}, Issac Goh^{1,2†} Antony Rose^{1,2‡}, Simone Webb^{1,2‡}, Justin
4 Engelbert¹, Yorick Gitton³, Emily Stephenson^{1,2}, Mariana Quiroga Londoño⁴, Michael
5 Mather¹, Nicole Mende⁴, Ivan Imaz-Rosshandler^{4,5}, Dave Horsfall¹, Daniela Basurto-
6 Lozada¹, Nana-Jane Chipampe², Victoria Rook², Pavel Mazin², MS Vijayabaskar⁴, Rebecca
7 Hannah⁴, Laure Gambardella², Kile Green⁶, Stephane Ballereau², Megumi Inoue³, Liz Tuck²,
8 Valentina Lorenzi², Kwasi Kwakwa², Clara Alsinet², Bayanne Olabi¹, Mohi Miah¹, Chloe
9 Admane^{1,2}, Dorin-Mirel Popescu¹, Meghan Acres¹, David Dixon¹, Rowen Coulthard⁷, Steven
10 Lisgo¹, Deborah J Henderson¹, Emma Dann², Chenqu Suo², Sarah J Kinston⁴, Jong-eun
11 Park⁸, Krzysztof Polanski², Stijn Van Dongen², Kerstin B Meyer², Marella de Bruijn⁹, James
12 Palis¹⁰, Sam Behjati^{2,11}, Elisa Laurenti⁴, Nicola K Wilson⁴, Roser Vento-Tormo², Alain
13 Chédotal³, Omer Bayraktar², Irene Roberts¹², Laura Jardine^{1*}, Berthold Göttgens^{4*}, Sarah A
14 Teichmann^{2*}, Muzlifah Haniffa^{2,1*}

15

16 †/‡ Equal contribution

17 * Corresponding authors. Email: mh32@sanger.ac.uk

18

19 **Affiliations:**

20 ¹Biosciences Institute, Newcastle University, NE2 4HH, UK

21 ²Wellcome Sanger Institute, Wellcome Genome Campus, Hinxton, Cambridge CB10 1SA,
22 UK

23 ³Sorbonne Université, INSERM, CNRS, Institut de la Vision, Paris, France

24 ⁴Department of Haematology, Wellcome-MRC Cambridge Stem Cell Institute, CB2 0AW,
25 UK

26 ⁵MRC Laboratory of Molecular Biology, Cambridge Biomedical Campus, CD2 0QH, UK

27 ⁶Translational and Clinical Research Institute, Newcastle University, NE2 4HH, UK

28 ⁷NovoPath, Department of Pathology, Newcastle Hospitals NHS Foundation Trust,

29 Newcastle upon Tyne, UK

30 ⁸Korea Advanced Institute of Science and Technology, Daejeon, South Korea

31 ⁹MRC Molecular Haematology Unit, MRC Weatherall Institute of Molecular Medicine,

32 Radcliffe Department of Medicine, University of Oxford, OX3 9DS, UK

33 ¹⁰Department of Pediatrics, University of Rochester Medical Center, Rochester, 14642, NY,

34 USA

35 ¹¹Department of Paediatrics, University of Cambridge, Cambridge, UK

36 ¹²Department of Paediatrics, University of Oxford, OX3 9DS, UK

37

38

39 **Abstract:** The yolk sac (YS) represents an evolutionarily-conserved extraembryonic structure
40 that ensures timely delivery of nutritional support and oxygen to the developing embryo.
41 However, the YS remains ill-defined in humans. We therefore assemble a complete single cell
42 3D map of human YS from 3-8 post conception weeks by integrating multiomic protein and
43 gene expression data. We reveal the YS as a site of primitive and definitive haematopoiesis
44 including a YS-specific accelerated route to macrophage production, a source of
45 nutritional/metabolic support and a regulator of oxygen-carrying capacity. We reconstruct the
46 emergence of primitive haematopoietic stem and progenitor cells from YS hemogenic
47 endothelium and their decline upon stromal support modulation as intraembryonic organs
48 specialise to assume these functions. The YS therefore functions as ‘three organs in one’
49 revealing a multifaceted relay of vital organismal functions as pregnancy proceeds.

50

51 **One Sentence Summary:** Human yolk sac is a key staging post in a relay of vital organismal
52 functions during human pregnancy.

53

54 **Main Text:**

55

56 The primary human YS derives from the hypoblast at around the time of embryo implantation
57 (Carnegie stage 4, CS4; ~1 post conception week (PCW)) (1, 2). A secondary YS beneath the
58 embryonic disc supersedes the primary structure at around CS6 (~2.5PCW) and persists until
59 8PCW (1, 2). The secondary YS surrounds a vitelline fluid-filled cavity with three tissue
60 compartments: mesothelium (a mesoderm-derived epithelial layer interfacing the amniotic
61 fluid), mesoderm (which contains an array of cell types, including endothelial cells, blood cells
62 and smooth muscle), and endoderm (interfacing the yolk sac cavity) (1). In phylogenetic terms,
63 the YS is first seen in vertebrates with yolk-rich eggs e.g., birds, reptiles and amphibians, where
64 its role is to extract macronutrients from yolk to sustain the embryo (3). The capacity to uptake,
65 transport and metabolise nutrients is retained in mouse and human YS (2). Haematopoiesis
66 originates in the YS in mammals, birds and some ray-finned fishes (4). The first wave of mouse
67 YS haematopoiesis (primitive) yields primitive erythroid cells, macrophages and
68 megakaryocytes from embryonic day 7.5 (E7.5) (4, 5). Following the onset of circulation, a
69 second wave of erytho-myeloid and lympho-myeloid progenitors arise in the YS and supply
70 the embryo (6). Finally, definitive haematopoietic stem cells arise in the aorta-gonad-
71 mesonephros (AGM) region of the dorsal aorta and seed the fetal liver.

72

73 Limited evidence suggests that YS also provides the first blood cells during development in
74 humans. Primitive erythroblasts expressing embryonic globin genes, surrounded by
75 endothelium, emerge at CS6 (~2.5PCW) (7, 8). YS also produces megakaryocytes, mast cells

76 and myeloid cells (9), although this has not yet been evidenced directly in functional studies.

77 Transplantation of human developmental tissues into immunodeficient mice has pinpointed the
78 origin of definitive haematopoietic stem and progenitor cells (HSPCs) (defined as long-term
79 multilineage repopulating cells) within the AGM region of embryo at CS14 (~5PCW) (10).

80 Equivalent cells are subsequently found in the YS at CS16 and in the liver from CS17 (10).

81 This sequence was also documented by following the transcriptional signature of definitive
82 HSPCs across organs (11). While the process of definitive HSPC emergence from hemogenic
83 endothelium (HE) has been reconstructed in human AGM (11, 12), the process by which earlier
84 progenitors arise in human YS has not been studied. Several key questions about human YS
85 haematopoiesis remain unanswered: what is the full repertoire of human YS-derived blood
86 cells, does the YS produce limited progenitors or HSPCs, do YS progenitors/HSPCs contribute
87 to long-lived populations such as tissue-resident macrophages, do YS progenitors/HSPCs arise
88 from HE, and what are the extrinsic regulators of this process.

89

90 In this study we report a time-resolved atlas of the human YS combining single cell multiomics
91 with 3D light-sheet microscopy and multiplex RNA *in situ* hybridisation, providing the first
92 comprehensive depiction of the metabolic and haematopoietic functions of the human YS, as
93 well as a benchmark for *in vitro* culture systems aiming to recapitulate early human
94 development.

95

96 **Results**

97

98 ***A single cell atlas of the human yolk sac***

99

100 We performed droplet-based scRNA-seq profiling of human YS, including both membrane and
101 contents, and integrated with external datasets to yield 169,798 high quality cells from 10
102 samples spanning 4-8PCW (CS10-CS23), which can be interrogated on our interactive web
103 portal (<https://developmental.cellatlas.io/yolk-sac>; password: ys2022) (13) (**Fig. 1A-C, S1A-C, Table S1-5**). All datasets used for cell state validation, *in vitro* iPSC culture and cross-
104 species comparisons are shown in **Fig. 1A (Table S6-7)**.

105

106

107 With iterative graph-based leiden clustering and annotation, the integrated YS scRNA-seq
108 dataset yielded 43 cell types, which we grouped into 15 broad categories including
109 haematopoietic cells, endoderm, mesoderm and mesothelium (**Fig. 1B-C, S1B-C, Table S3-5**). We consistently apply the term HSPC for cells expressing a core HSPC signature e.g. *CD34*,
110 *SPINK2*, *HLF*, without implying long-term repopulating capacity or multilineage potential.
111 With comparison datasets, unless otherwise specified, we adopt published annotations (**Table**
112 **S6-7**). We demonstrate the key marker genes for these broad cell categories, validated by plate-
113 based scRNA-seq (**Fig. S1D-E, Table S8, S5**) and surface protein expression from CITE-seq
114 analysis of n=2 YS cell suspension (**Fig. 1C, S1F-G, Table 9**). We used surface protein
115 expression data to construct a decision tree that identified combinatorial antibodies deployable
116 for YS cell type purification and functional characterisation (**Fig. S2A**). FACS isolation of
117 CD45⁻ cells with high scatter and Smart-seq2 analysis enabled enrichment and validation of
118 YS endoderm, mesothelium and erythroid cells (**Fig. S1D-E, Table S8, S5**). We generated
119 matched embryonic liver scRNA-seq data for established and late stage YS at CS18 and CS22-
120 matched embryonic liver scRNA-seq data for established and late stage YS at CS18 and CS22-

121 23 respectively (n=3; n=2 previously reported (9)) (**Fig. S2B-F**), validated by liver CITE-seq
122 data (**Fig. S3A-C, Table S10**), which confirmed the presence of pre-macrophages only in YS
123 and discrete B-cell progenitor stages only in the liver (**Fig. S1C, S3C**). Around half of YS
124 lymphoid cells were progenitors, which terminated in NK and ILC precursor states on force
125 directed graph (FDG) visualisation (**Fig. S3D**). A small population of cells were termed ‘B
126 lineage’ due to expression of *CD19*, *CD79B* and *IGLL1*. They did not express genes typical of
127 B1 cells (*CCR10*, *CD27*, *CD5*). Given the absence of distinct B cell progenitor stages and their
128 later emergence (>5PCW), these may constitute migratory B cells of fetal liver origin (**Fig.**
129 **S3D-E**).

130

131 To facilitate future use of our YS atlas, we employed a low-dimensional logistic regression
132 (LR) framework (see Methods). The trained LR models and weights from trained scVI models
133 are provided via our interactive web portal to enable mapping of scRNA-seq datasets using
134 CellTypist (14) and transfer learning with single-cell architectural surgery (scArches) (15),
135 respectively. Corresponding cross-tissue projection probability matrices are provided as
136 Supplementary Tables (**Table S11-18**).

137

138 Using selected marker genes and proteins from our droplet-based datasets (**Fig. 1C**), we
139 performed 3D visualisation of YS by light sheet microscopy, demonstrating the
140 $CD34^{hi}PVLAP^{hi}LYVE1^{lo}$ vitelline artery and a $CD34^{lo}PVLAP^{lo}LYVE1^{hi}$ vitelline vein
141 contiguous with a branching network of $CD34^{+}PVLAP^{lo}LYVE1^{hi}$ vessels within the YS (**Fig.**
142 **1D, Fig. S3F**). The $LYVE1^{hi}$ vessels localised within $HNF4A^{+}$ endoderm and adjacent to the
143 $ECAD^{+}$ mesothelium (**Fig. 1D, S3G-I**). Rare $IL7R^{+}$ lymphoid cells, and $CD1C^{+}C1QA^{+/-}$
144 dendritic cells (DCs) were identified within the mesoderm, while $ACTA2^{+}$ smooth muscle cells

145 surrounded *IL33*⁺ vessels, forming a sub-layer between mesoderm and *SPINK1*⁺ endoderm
146 (**Fig. 1E, S4A-B**).

147

148 To investigate the functional relevance of changes in YS cell composition during development,
149 we next assessed proportional representation of cell states by gestation. In early YS (CS10;
150 ~4PCW) HSPCs, erythroid cells, macrophages and megakaryocytes (MK) were the most
151 prevalent cell types with both HSPCs and MKs proportionately diminished thereafter, while
152 production of erythroid cells and macrophages was sustained. DC and *TREM2*⁺ microglia-like
153 cells did not emerge until >6PCW (**Fig. 1F, Table S4**). The ratio of haematopoietic to non-
154 haematopoietic cells was around 3:1 in early YS (CS10; ~4PCW), but with expansion of
155 fibroblasts particularly, the ratio in late YS (CS22-23; ~8PCW) approached 1:3 (**Fig. 1F**). We
156 performed graph-based differential abundance testing with Milo (16) to assess heterogeneity
157 within cell states by gestation. Both erythroid cells and macrophages had early and late-
158 gestation specific molecular states but MKs were transcriptionally homogenous across
159 gestation (**Fig. 1F, Table S19**). Early gestation molecular states were characterised by
160 significantly upregulated ribosomal and glycolytic genes (e.g., *RPS29*, *ENO1*, *LDHB*),
161 suggesting a common early burst of translation (**Fig. 1F, S4C, Table S4**). In contrast, cells at
162 later gestation upregulated specific lineage-defining genes compared to their earlier
163 counterparts (**Fig. 1F**).

164

165 ***Multi-organ functions of YS***

166

167 To probe the nutritional/metabolic functions of YS, we next focused our scRNA-seq analysis
168 on the non-haematopoietic cells. We identified an endoderm cell state co-expressing *APOA1/2*,
169 *APOC3* and *TTR*, similar to embryonic/fetal hepatocytes, which was present from gastrulation

170 (Fig. 2A, S4D, Table S3, S20, S7). Compared with embryonic liver hepatocytes, YS endoderm
171 expressed higher levels of transcripts for serine protease 3 (*PRSS3*), Glutathione S-Transferase
172 Alpha 2 (*GSTA2*) and multi-functional protein Galectin 3 (*LGALS3*), while embryonic liver
173 hepatocytes expressed a more extensive repertoire of detoxification enzymes, including alcohol
174 and aldehyde dehydrogenases (*ADH1A*, *ALDH1A1*) and cytochrome P450 enzymes involved
175 in metabolism of steroid hormones and vitamins (*CYP3A7*), fatty acids (*CYP4A11*) and the
176 conversion of cholesterol to bile acids (*CYP27A1*) (Fig. S4D, Table S20). YS endoderm and
177 embryonic liver hepatocytes shared gene modules implicated in coagulation and lipid and
178 glucose metabolism (Fig. 2B, Table S21). These modules were also conserved between human
179 and mouse extraembryonic endoderm (Fig. S4E-F, Table S21). We validated *in situ* the
180 expression of lipid transport (alpha-fetoprotein, albumin and alpha-1-antitrypsin) and
181 coagulation proteins (fibrin) in YS endoderm and embryonic liver hepatocytes (Fig. 2C, D).

182

183 We further explored the gene module ‘coagulation regulation’, conserved between YS and
184 liver, (Table S21) by examining expression of pro- and anticoagulant proteins across samples,
185 grouped by gestational age (Fig. 2D). From the earliest timepoints, YS endoderm expressed
186 components of the *F3* (Tissue factor)-activated coagulation pathway, particularly *F2*
187 (Thrombin) and *F10* (Factor X) and anticoagulant proteins *SERPINC1* (Antithrombin III) and
188 *PROS1* (Protein S) (Fig. 2D). Tissue factor, Antithrombin III and Fibrinogen subunits were
189 also expressed in mouse extraembryonic endoderm (Fig. S4E). Factors for the intrinsic
190 pathway (triggered by exposed collagen) were minimally expressed in YS, but were expressed
191 by embryonic liver hepatocytes (Fig. 2D). Given the importance of Tissue factor in YS
192 angiogenesis (17, 18), it is likely the coagulant and anticoagulant pathways develop in parallel
193 as a means to balance haemostasis.

194

195 In addition to their metabolic and coagulation functions, YS endoderm cells expressed EPO
196 and THPO that are critical for erythropoiesis and megakaryopoiesis (**Fig 2D, S4G**). EPO is
197 known to be produced by mouse YS endoderm (19), and both growth factors are produced by
198 human FL hepatocytes (9), but their combined presence has not previously been reported in
199 human YS.

200

201 We next investigated how multi-organ functions of YS endoderm change over time. Milo-
202 generated DEGs between early and late YS endoderm neighbourhoods revealed active retinoic
203 acid and lipid metabolic processes until 7PCW, after which genes associated with cell stress
204 and death were expressed (**Fig. 2E, Table S22**). Collectively, our findings describe a critical
205 role of the human YS to support haematopoiesis, metabolism, coagulation and erythroid cell
206 mass regulation, prior to these functions being taken over by fetal liver, and ultimately, by adult
207 liver (metabolism and coagulation), bone marrow (haematopoiesis) and kidney (erythroid cell
208 mass regulation) (**Fig. 2F**).

209

210 *Primitive versus definitive haematopoiesis in YS and liver*

211

212 Whether the YS is a site of definitive haematopoiesis in humans has not been fully resolved
213 (20). Human YS progenitors spanned two groups- HSPC characterised by *SPINK2*, *CYTL1* and
214 *HOXB9*, and cycling HSPC characterised by cell-cycle associated genes such as *MKI67* and
215 *TOP2A* (**Fig. S5A**). HSPC and cycling HSPC had the highest probability of class prediction to
216 fetal/embryonic liver HSC and MPP respectively (**Fig. S5B**). We further identified HSPC sub-
217 states expressing markers characteristic of primitive (*DDIT4*, *SLC2A3*, *RGS16*, *LIN28A*) and
218 definitive (*KIT*, *ITGA4*, *CD74*, *PROCR*) HSPCs in human YS/AGM (11), present in both
219 HSPC and cycling HSPC fractions (**Fig. 3A-C**). Both the primitive and definitive HSPC sub-

220 states expressed canonical HSPC genes such as *SPINK2*, *HOPX* and *HLF* but diverged in
221 expression of genes involved in multiple processes such as enzymes (*GADI*), growth factors
222 (*FGF23*), adhesion molecules (*SELL*) and patterning genes (*HOXA7*) (**Fig. 3A, S5C**).
223 Differential protein expression in CITE-seq data indicated that CD194 (CCR4), CD357 and
224 CD122 mark primitive HSPCs while CD197 (CCR7), CD193 and CD48 are preferentially
225 expressed on definitive HSPCs (**Fig. S5D**). We confirmed that an iPSC-derived culture system
226 reported to generate definitive HSPCs did express markers characteristic of definitive HSPCs
227 (*11*), but an iPSC-derived culture system optimised for macrophage production (*21*) did not
228 (**Fig. 3A**). To assess cross tissue HSPC heterogeneity, we integrated HSPCs across
229 hematopoietic organs (see Methods) (**Fig. 3C, S5E**). By kernel density estimation in integrated
230 UMAP embeddings, YS definitive HPSCs co-localized with definitive HSPCs from age-
231 matched liver (**Fig. 3C, S5E**). From exclusively primitive HSPCs at ~3PCW, we observed
232 rapid accumulation of definitive HSPCs after AGM development CS14 (~5PCW), likely
233 accounting for the increase in YS HSPC/progenitor fraction at 8PCW (**Fig. 1F, 3B, S5F**).

234
235 Next, we aimed to establish when the liver takes over from YS haematopoiesis and whether it
236 initially uses primitive or definitive HSPCs. Prior to AGM (and to circulation), the human
237 embryonic liver is macroscopically pale, suggesting that erythropoiesis predominantly occurs
238 in the YS (**Fig. 3D**). We tracked the proportional representation of haemoglobin (Hb) subtypes
239 over time as a proxy for YS versus embryonic liver contributions, as the zeta globin chain
240 (*HBZ*) is restricted to primitive erythroblasts while definitive erythroblasts in fetal liver express
241 gamma globins (*HBG1*) (22, 23) (**Fig. 3E**). Our observation of sustained *HBZ* production in
242 YS, for several days prior to liver bud formation (4 PCW), is consistent with a scenario where
243 YS supports sustained erythropoiesis. The minimal zeta globin expression and expression of
244 *HBZ* repressors by embryonic liver erythroblasts suggests that embryonic liver erythropoiesis

245 is predominantly definitive, as we have previously shown (9), and that the transition to liver-
246 dominated erythropoiesis occurs around 8PCW (**Fig. 3E**). This differs from the situation in
247 mice, whereby immature definitive erythroid progenitors exit the YS and rapidly mature in
248 other sites (24), as evidenced by the macroscopically red appearance of the mouse embryonic
249 liver prior to AGM maturation (**Fig. 3D**). Tracking Hb subtype usage in the mouse, we noted
250 two waves of erythropoiesis pre-AGM: primitive haematopoiesis in the YS (initially *Hbb BH1*
251 and *Hba X-Hba1*) and pro-definitive haematopoiesis mirrored in both YS and torso (*Hbb BT1*
252 and *Hbb BS*) (**Fig. S5G-I**).

253
254 Given the co-existence of primitive and definitive HSPCs in most of our YS samples, we
255 examined an earlier reference (prior to AGM-HSPC derivation) to explore the differentiation
256 potential of primitive HSPCs. At gastrulation (~3PCW), the YS haematopoietic landscape had
257 a tripartite differentiation structure, with erythroid, MK and myeloid differentiation (**Fig. 3F**).
258 This structure was also observed in mouse YS (**Fig. S6A-B, Table S13, S5**). A differential-
259 fate-prediction analysis demonstrated that primitive HSPCs pre-AGM at CS10-11 (~4PCW)
260 were biased towards myeloid cell fates, however the abundance of differentiating erythroid and
261 MK cells at this point suggests that an earlier wave of erythroid/MK production occurred (**Fig.**
262 **3G, S6C**). Post-AGM, the model predicted that remaining primitive HSPCs were
263 erythroid/MK-biased while definitive HSPCs were biased towards lymphoid and MK fates
264 (**Fig. 3G**). This is in keeping with the first appearance of YS lymphoid cells (ILC progenitors
265 and NK cells, and B lineage cells) post CS14 (**Fig. 1F**). Differential-fate-prediction analyses
266 revealed that iPSC-derived HSPCs were embryonic erythroid (i.e. erythroid cells expressing
267 *HBZ*), myeloid and MK-biased whilst definitive iPSC-derived HSPCs were lymphoid, MK,
268 non-embryonic erythroid and myeloid-primed, consistent with the predicted lineage potential
269 of their *in vivo* primitive and definitive counterparts (**Fig. 3H, S6D**).

270 ***The lifespan of YS HSPCs***

271

272 Following predictions that primitive HSPC differentiation potential changes over time, we
273 sought to examine the extrinsic support received by HSPCs across their lifespan. HSPCs arise
274 from hemogenic endothelium (HE) in the aorta, YS, bone marrow, placenta and embryonic
275 head in mice (25–29). In human AGM, definitive HSPCs have recently been shown to emerge
276 from *IL33⁺ALDH1A1⁺* arterial endothelial cells (AEC) via *KCNK17⁺ALDH1A1⁺* HE (12).

277 Dissecting YS endothelial cell (EC) states in greater detail, the broad category of PVLAP⁺ ECs
278 included AEC and HE, while LYVE1⁺ ECs encompassed sinusoidal, immature and VWF-
279 expressing ECs (**Fig. 4A, S7A-B, Table S4-5**). HE was a transient feature of early YS (**Fig.**
280 **4A**). Along inferred trajectories, YS HSPCs appeared to arise from AEC via HE as in AGM
281 (11), sequentially upregulating expected genes such as *ALDH1A1* (30) (**Fig. 4B**). The same EC
282 intermediate states and transition points could be identified in both iPSC culture systems (**Fig.**
283 **4B, S7C**). In keeping with their more recent endothelial origin, we found that YS HSPCs and
284 AGM HSPCs, but not embryonic liver or FBM HSPCs retained an EC gene signature
285 characterised by the expression of *KDR*, *CDH5*, *ESAM* and *PLVAP* (**Fig. 4C**)

286

287 Receptor-ligand interactions capable of supporting YS HSPC expansion and maintenance were
288 predicted using CellphoneDB (31). We identified ECs, fibroblasts, smooth muscle cells and
289 endoderm as likely interacting partners (**Fig. 4D-E, Table S23**). ECs were predicted to
290 maintain and support the HSPC pool through production of stem cell factor (KITLG) and
291 NOTCH 1/2 ligands DLL1 and JAG1 (32, 33) (**Fig. 4D**). ECs potentially expand the HSPC
292 pool via FN1 while fibroblasts and smooth muscle cells contribute via CSF1 and WNT5A (34–
293 36) (**Fig. 4D**). WNT5A may also regulate lineage specification in YS HSPC as non-canonical
294 WNT5A signalling promotes myelopoiesis at the expense of B lymphopoiesis in mouse (37).

295 Endoderm is predicted to interact with HSPCs *via* VTN and THPO, reported to promote
296 haematopoiesis and long-term-HSC-like quiescence, respectively (38, 39) (**Fig. 4D**).

297

298 Examining change in interactions over time, the key finding was diminishing interactions
299 between CS17-CS23 (4-8PCW) including loss of cytokine and growth factor support, loss of
300 TFG β , WNT and NOTCH2 signals by all stromal fractions (**Fig. 4D-E, S7D, Table S24**).

301 Many of these diminishing stromal ligands were still expressed in age-matched liver and AGM
302 stromal cells (**Fig. S7E, Table S24**). Adhesive interactions in YS were also predicted to be
303 significantly modulated (**Fig. S7F, Table S24**). While aged-matched liver provided
304 opportunities for adhesion with stromal cells, AGM did not (**Fig. S7F, Table S24**). Interactions
305 gained between CS17 and CS23 included endoderm-derived IL13 signalling to the *TMEM219*-
306 encoded receptor implicated in apoptosis-induction (**Fig. 4D**). While limited conclusions can
307 be made from studying cells that passed quality control for cell viability, we did observe
308 upregulation in pro-apoptotic gene scores in late stage YS HSPCs, both primitive and definitive
309 (**Fig. S7G**).

310

311 Despite marked change in the stromal environment of later stage YS, the proportion of HSPC
312 to cycling HSPC remained stable (**Fig. S5F**). Differential lineage priming analysis revealed
313 that very few HSPCs and mostly terminally differentiated cell states remained at CS22-
314 23/8PCW YS (**Fig. S6C**) Together these observations are in keeping with an early burst of
315 primitive HSPC production from transient YS HE, a later influx of definitive HSPCs derived
316 from AGM, a loss of stromal support between 6-8 PCW, resulting in apoptosis and depletion
317 of remaining HSPCs by terminal differentiation.

318

319

320 **An accelerated route to macrophage production in YS and iPSC culture**

321

322 While YS progenitors are restricted to a short time-window in early gestation, mouse models
323 suggest that they contribute to long-lived macrophage populations in some tissues (40). In our
324 YS data, non-progenitor myeloid cells (lacking *AZU1*, *PRTN3* and *MPO*) included *HMGB2*,
325 *LYZ* and *LSPI*-expressing promonocytes, pre-macrophages (expression profile below) and
326 *C1QA/B/C* and *MRC* macrophages (**Fig. S8A**). Monocytes were observed only after liver-bud
327 formation and AGM-derived haematopoiesis at CS14 (~5PCW) (**Fig. 5A**, **Fig. S8B**). A high
328 probability of class prediction between YS and embryonic liver monocytes was noted (**Fig. 5B**,
329 **Table S12**). A sub-population of YS monocytes (Monocyte2) expressed *ICAM3*, *SELL*, and
330 *PLAC8* (adhesion molecules expressed by embryonic liver but not YS HSPCs), in keeping with
331 liver-derived monocytes migrating to YS (**Fig. 5C**). However, sequential waves of
332 monopoiesis occurring within the YS cannot be excluded. YS CITE-seq data confirmed
333 differentiatial expression of *CD62L* (*SELL*) and *CD14* (*CD14*) on Monocyte2 compared to
334 Monocyte1 and identified additional discriminatory markers; e.g., *CD15*, *CD43* for Monocyte1
335 and *CD9*, *CD35* for Monocyte2 (**Fig. S8C**, **Table S25**).

336

337 The YS pre-macrophage uniquely expressed high levels of *PTGS2*, *MSL1* and *SPIA1*, as well
338 as expressing progenitor genes (*SPINK2*, *CD34*, *SMIM24*), macrophage genes (*C1QA*, *MRC1*),
339 and *CD52* which is typically associated with monocytes (**Fig. S8A**). This YS pre-macrophage
340 rapidly declined by 5PCW and had no equivalent in embryonic liver (**Fig. 5A-B**), which led us
341 to investigate putative macrophage differentiation trajectories in YS. FDG and partition-based
342 graph abstraction (PAGA) visualisation revealed a direct, monocyte-independent trajectory to
343 YS macrophages prior to CS14 (**Fig. 5D**). In this pre-AGM trajectory, a transition from cycling
344 HSPC to pre-macrophages, then macrophages (**Fig. 5D**) supports our predictions that primitive

345 pre-AGM HSPCs exhibit myeloid bias (**Fig. 3G**). After CS14, a clear differentiation trajectory
346 from cycling HSPC to monocytes and monocyte-macrophages was seen, but there were few
347 transitional cells connecting to macrophages (**Fig. 5D**). 15.33% of this macrophage pool was
348 proliferating and CellRank RNA state transition analysis was in keeping with active self-
349 renewal (**Fig. S8D**).

350

351 To explore how the two YS macrophage differentiation pathways are regulated, we examined
352 differential transcription factor (TF) usage with PySCENIC (**Fig. 5E, Table S26**). YS pre-
353 macrophages were predicted to use a group of TFs, including FLI1 and MEF2C, that have been
354 reported in the differentiation of multiple lineages (41, 42), whereas the monocyte-dependent
355 route (CMPs, MOP, promonocytes and monocytes) relied on recognised myeloid transcription
356 factors such as SPI1, CEBPA and IRF8 (**Fig. 5E**).

357

358 TREM2⁺ macrophages (43), which had a high probability of correlation with fetal brain
359 microglia (44), fetal skin TREM2⁺ (45) and fetal testes TREM2⁺ macrophages (46), were
360 observed in YS only after CS14 (**Fig. 5A, 5D, 5F, S8E, Table S18**). By FDG, PAGA and
361 CellRank RNA state transition analysis, TREM2⁺ macrophages were closely connected to the
362 self-renewing macrophage population (**Fig. 5D, S8D**). *In situ*, YS TREM2⁺ macrophages were
363 adjacent to the mesothelium, in a region enriched by EC (**Fig. S8F**). CellphoneDB predicted
364 interactions between TREM2⁺ macrophages and VWF⁺ EC, via CXCL8 and NRP1, both of
365 which are involved in angiogenic pathways (47, 48) (**Fig. 5G, Table S23**). TREM2⁺
366 macrophages also expressed the purinergic receptor P2RY12 that supports trafficking towards
367 ATP/ADP-expressing ECs, as reported in mouse CNS (49) (**Fig. 5F**).

368

369 In a recent dissection of mouse macrophage heterogeneity across tissues and time, TLF⁺
370 macrophages (emerging from YS progenitors both directly and via a fetal monocyte
371 intermediate) contributed to long-lived self-renewing tissue macrophage populations, while
372 CCR2⁺ and MHC-II^{hi} macrophage pools received continual input from monocytes (50). To
373 explore the contribution of YS-derived macrophages in prenatal human tissues, we interrogated
374 a human pan-fetal immune cell atlas (45) to explore the proportion of cells representing each
375 macrophage pool over gestational time (**Fig. S8G**). TLF⁺ cells first emerged in YS, and were
376 subsequently found in both liver and skin. The proportion of TLF⁺ macrophages decreased
377 over gestational time in all tissues, while the proportion of MHC-II^{hi} macrophages increased,
378 particularly after 10PCW. While our data cannot discern whether TLF⁺ macrophages are
379 upregulating an MHC-II^{hi} transcriptional programme or whether TLF⁺ macrophages are being
380 replaced by a second wave of monocyte-derived macrophages, we can conclude that the TLF⁺
381 signature, temporally consistent with a YS origin, does not persist in humans to the extent
382 observed in mouse (50). TLF⁺ macrophages in fetal liver were found within proliferating
383 Kupffer cells ('Kupffer 1' in Popescu *et al* (9)). Liver and YS CITE-seq data confirmed protein
384 expression of CD206 and CD163 in TLF⁺ macrophages and further identified CD28, CD49a,
385 TSLPR and CD144 as positive identification markers that are minimally expressed in
386 remaining Kupffer cells (**Fig. S8H, Table S27**).

387
388 As macrophage differentiation from iPSCs permits high-resolution sampling over time, we
389 sought to establish whether the macrophage subsets and developmental pathways we observed
390 were recapitulated *in vitro*. To this end, we integrated our YS gene expression data with
391 scRNA-seq data from iPSC-derived macrophage differentiation (n=19; k=50,512) by Alsinet
392 *et al* (21) after refining the annotations of iPSC-derived cell-states (see Methods) (**Fig. S9A-D**,
393 **Table S14, S5**). Non-adherent, CD14-expressing cells appearing after week 2 of differentiation

394 expressed *C1QA*, *C1QB* and *APOC1* in keeping with a macrophage identity, while *S100A8/9*,
395 *FCN1*, *CD52* and *CD14*-expressing monocytes only emerged after week 3 (**Fig. S9A-D**). Prior
396 to monocyte emergence, a monocyte-independent macrophage differentiation trajectory was
397 observed, consistent with the observations by Alsinet et al (21) (**Fig. 5H**, **Fig. S9A-D**). TF
398 regulatory profiles of iPSC-derived macrophage differentiation were consistent with both pre-
399 macrophage and monocyte-dependent *in vivo* TF profiles, including usage of *MEF2C*, *SPI1*,
400 *CEBPA* and *IRF8* in iPSC-derived pre-macrophages (**Fig. 5I**, **Table 26**). However, neither
401 system recapitulated TREM2⁺ macrophages suggesting that stromal cells, specifically ECs,
402 may be required to acquire the TREM2⁺ molecular profile.

403

404 **Discussion**

405

406 Using state-of-the-art single cell multiomic and imaging technologies we delineate the dynamic
407 composition and functions of human YS *in vivo* from the 3rd post conception week (PCW),
408 when the three embryonic germ layers form, to the 8th PCW when the majority of organ
409 structures are already established (22). We detail how the YS endoderm shares metabolic and
410 biosynthetic functions with liver and erythropoiesis-stimulating functions with liver and
411 kidney. In part, this shared functionality may relate to a common role in creating a niche for
412 haematopoiesis (51). Unlike in mice, where primitive erythroid progenitors mature in the YS
413 (prior to circulation being established) but erythromyeloid progenitors can exit the YS and
414 mature in the fetal liver, we show that active differentiation of erythroid and macrophage cells
415 occurs for several weeks in human YS, prior to liver handover. The multi-organ functions,
416 including extended haematopoiesis, of human YS may be an evolutionary adaptation to the
417 longer gestation in humans. While an earlier study in humans, based on colony assays,

418 suggested that the transition from YS to liver occurred at 5PCW, no YS samples were studied
419 after this point (52).

420

421 The developmental window investigated here encompasses haematopoiesis from HSPCs
422 arising both within the YS and within the embryo proper. We reconstruct YS HSPCs
423 emergence from a temporally-restricted HE, featuring similar transition states and molecular
424 regulation to AGM HSPCs. By gastrulation (CS7; ~3PCW), YS HSPCs already differentiate
425 into primitive erythroid, MK and myeloid lineages. Building on a recent compilation of gene
426 scorecards that characterise primitive and definitive HSPCs (11), we were able to parse the two
427 fractions and document transition to definitive HSPC-dominance after CS14 (~5PCW). This
428 separation also allowed us to identify a primitive HSPC bias towards myeloid, erythroid and
429 megakaryocyte lineages and a definitive HSPCs bias towards megakaryocyte and lymphoid
430 lineages. Both primitive and definitive HSPCs in the YS became more quiescent and
431 upregulated apoptosis-related genes between CS17 and CS23 (~6-8PCW). Stromal cell ligands
432 predicted to support HSPCs were markedly disrupted during this time, suggesting that the
433 barriers to the survival of YS HSPCS may be extrinsic.

434

435 Primitive HSPCs uniquely employ an accelerated route to macrophage production independent
436 of monocytes. The monocyte-dependent route may provide more tunable macrophage
437 production via circulating innate immune cells to facilitate macrophage regeneration in
438 response to tissue damage, inflammation or infection. While both primitive and definitive
439 HSPCs, ‘accelerated’ and monocyte-dependent macrophages were recapitulated during *in*
440 *vitro* differentiation of iPSCs, TREM2⁺ macrophages were not. TREM2⁺ macrophages, which
441 are transcriptionally aligned with brain microglia, fetal skin, testes and AGM TREM2⁺
442 macrophages, were predicted to interact with endothelial cells, potentially supporting

443 angiogenesis as described in mouse brain (44). Benchmarking of *in vitro* cultures against *in*
444 *vivo* cell states and trajectories can facilitate more faithful replication of early blood and
445 immune cells.

446

447 There is a growing appreciation of the potentially life-long consequences of early
448 developmental processes. Our study illuminates a previously obscure phase of human
449 development, where vital organismal functions are delivered by a transient extraembryonic
450 organ employing non-canonical cellular differentiation paths. It will be fascinating to explore
451 how these processes may impact on tissue homeostasis and disease across the human lifespan.

452 **References and Notes:**

453 1. C. Ross, T. E. Boroviak, Origin and function of the yolk sac in primate embryogenesis. *Nat. Commun.* **11**, 3760 (2020).

455 2. T. Cindrova-Davies, E. Jauniaux, M. G. Elliot, S. Gong, G. J. Burton, D. S. Charnock-Jones, RNA-seq reveals conservation of function among the yolk sacs of human, mouse, and chicken. *Proc. Natl. Acad. Sci. U. S. A.* **114**, E4753–E4761 (2017).

458 3. H. W. Mossman, *Vertebrate Fetal Membranes: Comparative Ontogeny and Morphology, Evolution, Phylogenetic Significance, Basic Functions, Research Opportunities* (1987).

460 4. T. Yamane, Mouse Yolk Sac Hematopoiesis. *Front. Cell Dev. Biol.* **0** (2018), doi:10.3389/fcell.2018.00080.

462 5. J. Palis, J. Malik, K. E. McGrath, P. D. Kingsley, Primitive erythropoiesis in the mammalian embryo. *The International Journal of Developmental Biology.* **54** (2010), pp. 1011–1018.

464 6. G. Canu, C. Ruhrberg, First blood: the endothelial origins of hematopoietic progenitors. *Angiogenesis.* **24** (2021), pp. 199–211.

466 7. M. Tavian, M. F. Hallais, B. Péault, Emergence of intraembryonic hematopoietic precursors in the pre-liver human embryo. *Development.* **126**, 793–803 (1999).

468 8. C. Peschle, A. R. Migliaccio, G. Migliaccio, M. Petrini, M. Calandrini, G. Russo, G. Mastroberardino, M. Presta, A. M. Gianni, P. Comi, Embryonic---Fetal Hb switch in humans: studies on erythroid bursts generated by embryonic progenitors from yolk sac and liver. *Proc. Natl. Acad. Sci. U. S. A.* **81**, 2416–2420 (1984).

472 9. D.-M. Popescu, R. A. Botting, E. Stephenson, K. Green, S. Webb, L. Jardine, E. F. Calderbank, K. Polanski, I. Goh, M. Efremova, M. Acres, D. Maunder, P. Vegh, Y. Gitton, J.-E. Park, R. Vento-Tormo, Z. Miao, D. Dixon, R. Rowell, D. McDonald, J. Fletcher, E. Poyner, G. Reynolds, M. Mather, C. Moldovan, L. Mamanova, F. Greig, M. D. Young, K. B. Meyer, S. Lisgo, J.

476 Bacardit, A. Fuller, B. Millar, B. Innes, S. Lindsay, M. J. T. Stubbington, M. S. Kowalczyk, B.

477 Li, O. Ashenberg, M. Tabaka, D. Dionne, T. L. Tickle, M. Slyper, O. Rozenblatt-Rosen, A.

478 Filby, P. Carey, A.-C. Villani, A. Roy, A. Regev, A. Chédotal, I. Roberts, B. Göttgens, S.

479 Behjati, E. Laurenti, S. A. Teichmann, M. Haniffa, Decoding human fetal liver haematopoiesis.

480 *Nature*. **574**, 365–371 (2019).

481 10. A. Ivanovs, S. Rybtsov, L. Welch, R. A. Anderson, M. L. Turner, A. Medvinsky, Highly potent

482 human hematopoietic stem cells first emerge in the intraembryonic aorta-gonad-mesonephros

483 region. *J. Exp. Med.* **208**, 2417–2427 (2011).

484 11. V. Calvanese, S. Capellera-Garcia, F. Ma, I. Fares, S. Liebscher, E. S. Ng, S. Ekstrand, J.

485 Aguadé-Gorgorió, A. Vavilina, D. Lefaudeux, B. Nadel, J. Y. Li, Y. Wang, L. K. Lee, R.

486 Ardehali, M. L. Iruela-Arispe, M. Pellegrini, E. G. Stanley, A. G. Elefanty, K. Schenke-Layland,

487 H. K. A. Mikkola, Mapping human haematopoietic stem cells from haemogenic endothelium to

488 birth. *Nature*. **604**, 534–540 (2022).

489 12. Y. Zeng, J. He, Z. Bai, Z. Li, Y. Gong, C. Liu, Y. Ni, J. Du, C. Ma, L. Bian, Y. Lan, B. Liu,

490 Tracing the first hematopoietic stem cell generation in human embryo by single-cell RNA

491 sequencing. *Cell Res.* **29**, 881–894 (2019).

492 13. D. Horsfall, J. McGrath, Adifa software for Single Cell Insights (2022),

493 doi:10.5281/zenodo.5824896.

494 14. C. Domínguez Conde, C. Xu, L. B. Jarvis, D. B. Rainbow, S. B. Wells, T. Gomes, S. K. Howlett,

495 O. Suchanek, K. Polanski, H. W. King, L. Mamanova, N. Huang, P. A. Szabo, L. Richardson, L.

496 Bolt, E. S. Fasouli, K. T. Mahbubani, M. Prete, L. Tuck, N. Richoz, Z. K. Tuong, L. Campos, H.

497 S. Mousa, E. J. Needham, S. Pritchard, T. Li, R. Elmentait, J. Park, E. Rahmani, D. Chen, D. K.

498 Menon, O. A. Bayraktar, L. K. James, K. B. Meyer, N. Yosef, M. R. Clatworthy, P. A. Sims, D.

499 L. Farber, K. Saeb-Parsy, J. L. Jones, S. A. Teichmann, Cross-tissue immune cell analysis

500 reveals tissue-specific features in humans. *Science*. **376**, eabl5197 (2022).

501 15. M. Lotfollahi, M. Naghipourfar, M. D. Luecken, M. Khajavi, M. Büttner, M. Wagenstetter, Ž.
502 Avsec, A. Gayoso, N. Yosef, M. Interlandi, S. Rybakov, A. V. Misharin, F. J. Theis, Mapping
503 single-cell data to reference atlases by transfer learning. *Nat. Biotechnol.* **40**, 121–130 (2022).

504 16. E. Dann, N. C. Henderson, S. A. Teichmann, M. D. Morgan, J. C. Marioni, Differential
505 abundance testing on single-cell data using k-nearest neighbor graphs. *Nat. Biotechnol.* (2021),
506 doi:10.1038/s41587-021-01033-z.

507 17. J. Xue, Q. Wu, L. A. Westfield, E. A. Tuley, D. Lu, Q. Zhang, K. Shim, X. Zheng, J. E. Sadler,
508 Incomplete embryonic lethality and fatal neonatal hemorrhage caused by prothrombin deficiency
509 in mice. *Proc. Natl. Acad. Sci. U. S. A.* **95**, 7603–7607 (1998).

510 18. W. Ruf, N. Yokota, F. Schaffner, Tissue factor in cancer progression and angiogenesis.
511 *Thrombosis Research*. **125** (2010), pp. S36–S38.

512 19. Y. Yasuda, M. Okano, M. Nagao, S. Masuda, H. Konishi, K. Ueda, T. Matsuo, K. Tsujiguchi, S.
513 Tajima, R. Sasaki, T. Tanimura, Erythropoietin in mouse avascular yolk sacs is increased by
514 retinoic acid. *Dev. Dyn.* **207**, 184–194 (1996).

515 20. J. Palis, M. C. Yoder, Yolk-sac hematopoiesis: the first blood cells of mouse and man. *Exp.*
516 *Hematol.* **29**, 927–936 (2001).

517 21. C. Alsinet, M. N. Primo, V. Lorenzi, E. Bello, I. Kelava, C. P. Jones, R. Vilarrasa-Blasi, C.
518 Sancho-Serra, A. J. Knights, J.-E. Park, B. S. Wyspianska, G. Trynka, D. F. Tough, A. Bassett,
519 D. J. Gaffney, D. Alvarez-Errico, R. Vento-Tormo, Robust temporal map of human in vitro
520 myelopoiesis using single-cell genomics. *Nat. Commun.* **13**, 1–17 (2022).

521 22. C. Peschle, F. Mavilio, A. Carè, G. Migliaccio, A. R. Migliaccio, G. Salvo, P. Samoggia, S.
522 Petti, R. Guerriero, M. Marinucci, Haemoglobin switching in human embryos: asynchrony of
523 zeta----alpha and epsilon----gamma-globin switches in primitive and definite erythropoietic
524 lineage. *Nature*. **313**, 235–238 (1985).

525 23. J. Palis, Primitive and definitive erythropoiesis in mammals. *Frontiers in Physiology*. **5** (2014), ,
526 doi:10.3389/fphys.2014.00003.

527 24. K. McGrath, J. Palis, Ontogeny of erythropoiesis in the mammalian embryo. *Curr. Top. Dev.*
528 *Biol.* **82**, 1–22 (2008).

529 25. T. Jaffredo, R. Gautier, A. Eichmann, F. Dieterlen-Lièvre, Intraaortic hemopoietic cells are
530 derived from endothelial cells during ontogeny. *Development*. **125**, 4575–4583 (1998).

531 26. L. Yvernogea, R. Gautier, L. Petit, H. Khoury, F. Relaix, V. Ribes, H. Sang, P. Charbord, M.
532 Souyri, C. Robin, T. Jaffredo, In vivo generation of haematopoietic stem/progenitor cells from
533 bone marrow-derived haemogenic endothelium. *Nat. Cell Biol.* **21**, 1334–1345 (2019).

534 27. Z. Li, Y. Lan, W. He, D. Chen, J. Wang, F. Zhou, Y. Wang, H. Sun, X. Chen, C. Xu, S. Li, Y.
535 Pang, G. Zhang, L. Yang, L. Zhu, M. Fan, A. Shang, Z. Ju, L. Luo, Y. Ding, W. Guo, W. Yuan,
536 X. Yang, B. Liu, Mouse Embryonic Head as a Site for Hematopoietic Stem Cell Development.
537 *Cell Stem Cell*. **11** (2012), pp. 663–675.

538 28. J. M. Frame, K. H. Fegan, S. J. Conway, K. E. McGrath, J. Palis, Definitive Hematopoiesis in
539 the Yolk Sac Emerges from Wnt-Responsive Hemogenic Endothelium Independently of
540 Circulation and Arterial Identity. *Stem Cells*. **34**, 431–444 (2016).

541 29. K. E. Rhodes, C. Gekas, Y. Wang, C. T. Lux, C. S. Francis, D. N. Chan, S. Conway, S. H. Orkin,
542 M. C. Yoder, H. K. A. Mikkola, The emergence of hematopoietic stem cells is initiated in the
543 placental vasculature in the absence of circulation. *Cell Stem Cell*. **2**, 252–263 (2008).

544 30. R. Thambyrajah, M. Mazan, R. Patel, V. Moignard, M. Stefanska, E. Marinopoulou, Y. Li, C.
545 Lancrin, T. Clapes, T. Möröy, C. Robin, C. Miller, S. Cowley, B. Göttgens, V. Kouskoff, G.
546 Lacaud, GFI1 proteins orchestrate the emergence of haematopoietic stem cells through
547 recruitment of LSD1. *Nat. Cell Biol.* **18**, 21–32 (2016).

548 31. M. Efremova, M. Vento-Tormo, S. A. Teichmann, R. Vento-Tormo, CellPhoneDB v2.0:

549 Inferring cell-cell communication from combined expression of multi-subunit receptor-ligand
550 complexes, , doi:10.1101/680926.

551 32. L. Jardine, S. Webb, I. Goh, M. Quiroga Londoño, G. Reynolds, M. Mather, B. Olabi, E.
552 Stephenson, R. A. Botting, D. Horsfall, J. Engelbert, D. Mauder, N. Mende, C. Murnane, E.
553 Dann, J. McGrath, H. King, I. Kucinski, R. Queen, C. D. Carey, C. Shrubssole, E. Poyner, M.
554 Acres, C. Jones, T. Ness, R. Coulthard, N. Elliott, S. O'Byrne, M. L. R. Haltalli, J. E. Lawrence,
555 S. Lisgo, P. Balogh, K. B. Meyer, E. Prigmore, K. Ambridge, M. S. Jain, M. Efremova, K.
556 Pickard, T. Creasey, J. Bacardit, D. Henderson, J. Coxhead, A. Filby, R. Hussain, D. Dixon, D.
557 McDonald, D.-M. Popescu, M. S. Kowalczyk, B. Li, O. Ashenberg, M. Tabaka, D. Dionne, T. L.
558 Tickle, M. Slyper, O. Rozenblatt-Rosen, A. Regev, S. Behjati, E. Laurenti, N. K. Wilson, A.
559 Roy, B. Göttgens, I. Roberts, S. A. Teichmann, M. Haniffa, Blood and immune development in
560 human fetal bone marrow and Down syndrome. *Nature*. **598**, 327–331 (2021).

561 33. J. Fröbel, T. Landspersky, G. Percin, C. Schreck, S. Rahmig, A. Ori, D. Nowak, M. Essers, C.
562 Waskow, R. A. J. Oostendorp, The Hematopoietic Bone Marrow Niche Ecosystem. *Front Cell
563 Dev Biol.* **9**, 705410 (2021).

564 34. P. Zhang, C. Zhang, J. Li, J. Han, X. Liu, H. Yang, The physical microenvironment of
565 hematopoietic stem cells and its emerging roles in engineering applications. *Stem Cell Res. Ther.*
566 **10**, 327 (2019).

567 35. S. Kaur, A. Sehgal, A. C. Wu, S. M. Millard, L. Batoon, C. J. Sandrock, M. Ferrari-Cestari, J.-P.
568 Levesque, D. A. Hume, L. J. Raggatt, A. R. Pettit, Stable colony-stimulating factor 1 fusion
569 protein treatment increases hematopoietic stem cell pool and enhances their mobilisation in mice.
570 *J. Hematol. Oncol.* **14**, 3 (2021).

571 36. B. Murdoch, K. Chadwick, M. Martin, F. Shojaei, K. V. Shah, L. Gallacher, R. T. Moon, M.
572 Bhatia, Wnt-5A augments repopulating capacity and primitive hematopoietic development of
573 human blood stem cells in vivo. *Proc. Natl. Acad. Sci. U. S. A.* **100**, 3422–3427 (2003).

574 37. H. Liang, Q. Chen, A. H. Coles, S. J. Anderson, G. Pihan, A. Bradley, R. Gerstein, R. Jurecic, S.
575 N. Jones, Wnt5a inhibits B cell proliferation and functions as a tumor suppressor in
576 hematopoietic tissue. *Cancer Cell*. **4**, 349–360 (2003).

577 38. J. Shen, Y. Zhu, S. Zhang, S. Lyu, C. Lyu, Z. Feng, D. L. Hoyle, Z. Z. Wang, T. Cheng,
578 Vitronectin-activated $\alpha v\beta 3$ and $\alpha v\beta 5$ integrin signalling specifies haematopoietic fate in human
579 pluripotent stem cells. *Cell Prolif*. **54**, e13012 (2021).

580 39. H. Yoshihara, F. Arai, K. Hosokawa, T. Hagiwara, K. Takubo, Y. Nakamura, Y. Gomei, H.
581 Iwasaki, S. Matsuoka, K. Miyamoto, H. Miyazaki, T. Takahashi, T. Suda, Thrombopoietin/MPL
582 signaling regulates hematopoietic stem cell quiescence and interaction with the osteoblastic
583 niche. *Cell Stem Cell*. **1**, 685–697 (2007).

584 40. F. Ginhoux, M. Guilliams, Tissue-Resident Macrophage Ontogeny and Homeostasis. *Immunity*.
585 **44**, 439–449 (2016).

586 41. C. Gekas, K. E. Rhodes, L. M. Gereige, H. Helgadottir, R. Ferrari, S. K. Kurdistani, E.
587 Montecino-Rodriguez, R. Bassel-Duby, E. Olson, A. V. Krivtsov, S. Armstrong, S. H. Orkin, M.
588 Pellegrini, H. K. A. Mikkola, Mef2C is a lineage-restricted target of Scl/Tal1 and regulates
589 megakaryopoiesis and B-cell homeostasis. *Blood*. **113**, 3461–3471 (2009).

590 42. E. Suzuki, S. Williams, S. Sato, G. Gilkeson, D. K. Watson, X. K. Zhang, The transcription
591 factor Fli-1 regulates monocyte, macrophage and dendritic cell development in mice.
592 *Immunology*. **139**, 318–327 (2013).

593 43. F. Wang, P. Ding, X. Liang, X. Ding, C. B. Brandt, E. Sjöstedt, J. Zhu, S. Bolund, L. Zhang, L.
594 P. M. H. de Rooij, L. Luo, Y. Wei, W. Zhao, Z. Lv, J. Haskó, R. Li, Q. Qin, Y. Jia, W. Wu, Y.
595 Yuan, M. Pu, H. Wang, A. Wu, L. Xie, P. Liu, F. Chen, J. Herold, J. Kalucka, M. Karlsson, X.
596 Zhang, R. B. Helmig, L. Fagerberg, C. Lindskog, F. Pontén, M. Uhlen, L. Bolund, N. Jessen, H.
597 Jiang, X. Xu, H. Yang, P. Carmeliet, J. Mulder, D. Chen, L. Lin, Y. Luo, Endothelial cell
598 heterogeneity and microglia regulons revealed by a pig cell landscape at single-cell level. *Nat.*

599 *Commun.* **13**, 1–18 (2022).

600 44. U. C. Eze, A. Bhaduri, M. Haeussler, T. J. Nowakowski, A. R. Kriegstein, Single-cell atlas of
601 early human brain development highlights heterogeneity of human neuroepithelial cells and early
602 radial glia. *Nat. Neurosci.* **24**, 584–594 (2021).

603 45. C. Suo, E. Dann, I. Goh, L. Jardine, V. Kleshchevnikov, J.-E. Park, R. A. Botting, E.
604 Stephenson, J. Engelbert, Z. K. Tuong, K. Polanski, N. Yayon, C. Xu, O. Suchanek, R.
605 Elmentaita, C. Domínguez Conde, P. He, S. Pritchard, M. Miah, C. Moldovan, A. S. Steemers, P.
606 Mazin, M. Prete, D. Horsfall, J. C. Marioni, M. R. Clatworthy, M. Haniffa, S. A. Teichmann,
607 Mapping the developing human immune system across organs. *Science*. **376**, eabo0510 (2022).

608 46. R. Vento-Tormo, L. Garcia-Alonso, V. Lorenzi, C. Mazzeo, C. Sancho-Serra, K. Roberts, J.
609 Engelbert, J. Alves-Lopes, M. Marečková, R. Botting, T. Li, B. Crespo, S. van Dongen, V.
610 Kiselev, E. Prigmore, A. Moffett, M. Herbert, O. A. Bayraktar, A. Surani, M. Haniffa, Single-
611 cell roadmap of human gonadal development (2021), doi:10.21203/rs.3.rs-496470/v1.

612 47. M. L. Petreaca, M. Yao, Y. Liu, K. DeFea, M. Martins-Green, Transactivation of Vascular
613 Endothelial Growth Factor Receptor-2 by Interleukin-8 (IL-8/CXCL8) Is Required for IL-
614 8/CXCL8-induced Endothelial Permeability. *Mol. Biol. Cell* (2007), doi:10.1091/mbc.e07-01-
615 0004.

616 48. Z. Lyu, H. Jin, Z. Yan, K. Hu, H. Jiang, H. Peng, H. Zhuo, Effects of NRP1 on angiogenesis and
617 vascular maturity in endothelial cells are dependent on the expression of SEMA4D. *Int. J. Mol.*
618 *Med.* **46**, 1321–1334 (2020).

619 49. K. Bisht, K. A. Okojie, K. Sharma, D. H. Lentferink, Y.-Y. Sun, H.-R. Chen, J. O. Uweru, S.
620 Amancherla, Z. Calcuttawala, A. B. Campos-Salazar, B. Corliss, L. Jabbour, J. Benderoth, B.
621 Friestad, W. A. Mills 3rd, B. E. Isakson, M.-È. Tremblay, C.-Y. Kuan, U. B. Eyo, Capillary-
622 associated microglia regulate vascular structure and function through PAXN1-P2RY12 coupling
623 in mice. *Nat. Commun.* **12**, 5289 (2021).

624 50. S. A. Dick, A. Wong, H. Hamidzada, S. Nejat, R. Nechanitzky, S. Vohra, B. Mueller, R. Zaman,
625 C. Kantores, L. Aronoff, A. Momen, D. Nechanitzky, W. Y. Li, P. Ramachandran, S. Q. Crome,
626 B. Becher, M. I. Cybulsky, F. Billia, S. Keshavjee, S. Mital, C. S. Robbins, T. W. Mak, S.
627 Epelman, Three tissue resident macrophage subsets coexist across organs with conserved origins
628 and life cycles. *Sci Immunol.* **7**, eabf7777 (2022).

629 51. S. Chou, H. F. Lodish, Fetal liver hepatic progenitors are supportive stromal cells for
630 hematopoietic stem cells. *Proc. Natl. Acad. Sci. U. S. A.* **107** (2010),
631 doi:10.1073/pnas.1003586107.

632 52. G. Migliaccio, A. R. Migliaccio, S. Petti, F. Mavilio, G. Russo, D. Lazzaro, U. Testa, M.
633 Marinucci, C. Peschle, Human embryonic hemopoiesis. Kinetics of progenitors and precursors
634 underlying the yolk sac----liver transition. *Journal of Clinical Investigation.* **78** (1986), pp. 51–
635 60.

636 53. H. Wang, J. He, C. Xu, X. Chen, H. Yang, S. Shi, C. Liu, Y. Zeng, D. Wu, Z. Bai, M. Wang, Y.
637 Wen, P. Su, M. Xia, B. Huang, C. Ma, L. Bian, Y. Lan, T. Cheng, L. Shi, B. Liu, J. Zhou,
638 Decoding Human Megakaryocyte Development. *Cell Stem Cell.* **28**, 535–549.e8 (2021).

639 54. L. Jardine, S. Webb, I. Goh, M. Quiroga Londoño, G. Reynolds, M. Mather, B. Olabi, E.
640 Stephenson, R. A. Botting, D. Horsfall, J. Engelbert, D. Maunder, N. Mende, C. Murnane, E.
641 Dann, J. McGrath, H. King, I. Kucinski, R. Queen, C. D. Carey, C. Shrubssole, E. Poyner, M.
642 Acres, C. Jones, T. Ness, R. Coulthard, N. Elliott, S. O’Byrne, M. L. R. Haltalli, J. E. Lawrence,
643 S. Lisgo, P. Balogh, K. B. Meyer, E. Prigmore, K. Ambridge, M. S. Jain, M. Efremova, K.
644 Pickard, T. Creasey, J. Bacardit, D. Henderson, J. Coxhead, A. Filby, R. Hussain, D. Dixon, D.
645 McDonald, D.-M. Popescu, M. S. Kowalczyk, B. Li, O. Ashenberg, M. Tabaka, D. Dionne, T. L.
646 Tickle, M. Slyper, O. Rozenblatt-Rosen, A. Regev, S. Behjati, E. Laurenti, N. K. Wilson, A.
647 Roy, B. Göttgens, I. Roberts, S. A. Teichmann, M. Haniffa, Blood and immune development in
648 human fetal bone marrow and Down syndrome. *Nature.* **598**, 327–331 (2021).

649 55. B. J. Stewart, J. R. Ferdinand, M. D. Young, T. J. Mitchell, K. W. Loudon, A. M. Riding, N.
650 Richoz, G. L. Frazer, J. U. L. Staniforth, F. A. Vieira Braga, R. A. Botting, D.-M. Popescu, R.
651 Vento-Tormo, E. Stephenson, A. Cagan, S. J. Farndon, K. Polanski, M. Efremova, K. Green, M.
652 Del Castillo Velasco-Herrera, C. Guzzo, G. Collord, L. Mamanova, T. Aho, J. N. Armitage, A.
653 C. P. Riddick, I. Mushtaq, S. Farrell, D. Rampling, J. Nicholson, A. Filby, J. Burge, S. Lisgo, S.
654 Lindsay, M. Bajenoff, A. Y. Warren, G. D. Stewart, N. Sebire, N. Coleman, M. Haniffa, S. A.
655 Teichmann, S. Behjati, M. R. Clatworthy, Spatiotemporal immune zonation of the human
656 kidney. *Science*. **365**, 1461–1466 (2019).

657 56. G. L. Website, Tracking Early Mammalian Organogenesis – Prediction and Validation of
658 Differentiation Trajectories at Whole Organism Scale. *ExtendedMouseAtlas*, (available at
659 <https://marionilab.github.io/ExtendedMouseAtlas/>).

660 57. R. C. V. Tyser, E. Mahammadov, S. Nakanoh, L. Vallier, A. Scialdone, S. Srinivas, Single-cell
661 transcriptomic characterization of a gastrulating human embryo. *Nature*. **600**, 285–289 (2021).

662 58. E. I. Crosse, S. Gordon-Keylock, S. Rybtsov, A. Binagui-Casas, H. Felchle, N. C. Nnadi, K.
663 Kirschner, T. Chandra, S. Tamagno, D. J. Webb, F. Rossi, R. A. Anderson, A. Medvinsky,
664 Multi-layered Spatial Transcriptomics Identify Secretory Factors Promoting Human
665 Hematopoietic Stem Cell Development. *Cell Stem Cell*. **27**, 822–839.e8 (2020).

666 59. T. Strachan, S. Lindsay, D. I. Wilson, *Molecular Genetics of Early Human Development* (Taylor
667 & Francis, 1997).

668 60. M. Belle, D. Godefroy, G. Couly, S. A. Malone, F. Collier, P. Giacobini, A. Chédotal,
669 Tridimensional Visualization and Analysis of Early Human Development. *Cell*. **169**, 161–
670 173.e12 (2017).

671 61. A.-C. Villani, R. Satija, G. Reynolds, S. Sarkizova, K. Shekhar, J. Fletcher, M. Griesbeck, A.
672 Butler, S. Zheng, S. Lazo, L. Jardine, D. Dixon, E. Stephenson, E. Nilsson, I. Grundberg, D.
673 McDonald, A. Filby, W. Li, P. L. De Jager, O. Rozenblatt-Rosen, A. A. Lane, M. Haniffa, A.

674 Regev, N. Hacohen, Single-cell RNA-seq reveals new types of human blood dendritic cells,
675 monocytes, and progenitors. *Science*. **356** (2017), doi:10.1126/science.aah4573.

676 62. S. L. Wolock, R. Lopez, A. M. Klein, Scrublet: Computational Identification of Cell Doublets in
677 Single-Cell Transcriptomic Data. *Cell Syst.* **8**, 281–291.e9 (2019).

678 63. S. J. Fleming, J. C. Marioni, M. Babadi, CellBender remove-background: a deep generative
679 model for unsupervised removal of background noise from scRNA-seq datasets, ,
680 doi:10.1101/791699.

681 64. F. A. Wolf, F. Alexander Wolf, P. Angerer, F. J. Theis, SCANPY: large-scale single-cell gene
682 expression data analysis. *Genome Biology*. **19** (2018), , doi:10.1186/s13059-017-1382-0.

683 65. M. P. Mulè, A. J. Martins, J. S. Tsang, Normalizing and denoising protein expression data from
684 droplet-based single cell profiling, , doi:10.1101/2020.02.24.963603.

685 66. R. Lopez, J. Regier, M. B. Cole, M. I. Jordan, N. Yosef, Deep generative modeling for single-
686 cell transcriptomics. *Nat. Methods*. **15**, 1053–1058 (2018).

687 67. A. Gayoso, R. Lopez, G. Xing, P. Boyeau, V. Valiollah Pour Amiri, J. Hong, K. Wu, M.
688 Jayasuriya, E. Mehlman, M. Langevin, Y. Liu, J. Samaran, G. Misrachi, A. Nazaret, O. Clivio,
689 C. Xu, T. Ashuach, M. Gabitto, M. Lotfollahi, V. Svensson, E. da Veiga Beltrame, V.
690 Kleshchevnikov, C. Talavera-López, L. Pachter, F. J. Theis, A. Streets, M. I. Jordan, J. Regier,
691 N. Yosef, A Python library for probabilistic analysis of single-cell omics data. *Nat. Biotechnol.*
692 **40**, 163–166 (2022).

693 68. I. Korsunsky, N. Millard, J. Fan, K. Slowikowski, F. Zhang, K. Wei, Y. Baglaenko, M. Brenner,
694 P.-R. Loh, S. Raychaudhuri, Fast, sensitive and accurate integration of single-cell data with
695 Harmony. *Nat. Methods*. **16**, 1289–1296 (2019).

696 69. M. Büttner, Z. Miao, F. A. Wolf, S. A. Teichmann, F. J. Theis, A test metric for assessing single-
697 cell RNA-seq batch correction. *Nat. Methods*. **16**, 43–49 (2019).

698 70. V. A. Traag, L. Waltman, N. J. van Eck, From Louvain to Leiden: guaranteeing well-connected
699 communities. *Sci. Rep.* **9**, 1–12 (2019).

700 71. C. D. Conde, C. Domínguez Conde, C. Xu, L. B. Jarvis, T. Gomes, S. K. Howlett, D. B.
701 Rainbow, O. Suchanek, H. W. King, L. Mamanova, K. Polanski, N. Huang, E. S. Fasouli, K. T.
702 Mahbubani, M. Prete, L. Tuck, N. Richoz, Z. K. Tuong, L. Campos, H. S. Mousa, E. J.
703 Needham, S. Pritchard, T. Li, R. Elmentaitaite, J. Park, D. K. Menon, O. A. Bayraktar, L. K. James,
704 K. B. Meyer, M. R. Clatworthy, K. Saeb-Parsy, J. L. Jones, S. A. Teichmann, Cross-tissue
705 immune cell analysis reveals tissue-specific adaptations and clonal architecture in humans, ,
706 doi:10.1101/2021.04.28.441762.

707 72. A. J. Tarashansky, J. M. Musser, M. Khariton, P. Li, D. Arendt, S. R. Quake, B. Wang, Mapping
708 single-cell atlases throughout Metazoa unravels cell type evolution. *Elife.* **10** (2021),
709 doi:10.7554/eLife.66747.

710 73. A. Edelstein, N. Amodaj, K. Hoover, R. Vale, N. Stuurman, Computer Control of Microscopes
711 Using µManager. *Current Protocols in Molecular Biology.* **92** (2010), ,
712 doi:10.1002/0471142727.mb1420s92.

713 74. D. Hörl, F. Rojas Rusak, F. Preusser, P. Tillberg, N. Randel, R. K. Chhetri, A. Cardona, P. J.
714 Keller, H. Harz, H. Leonhardt, M. Treier, S. Preibisch, BigStitcher: reconstructing high-
715 resolution image datasets of cleared and expanded samples. *Nat. Methods.* **16**, 870–874 (2019).

716 75. M. Gataric, J. S. Park, T. Li, V. Vaskivskyi, J. Svedlund, C. Strell, K. Roberts, M. Nilsson, L. R.
717 Yates, O. Bayraktar, M. Gerstung, PoSTcode: Probabilistic image-based spatial transcriptomics
718 decoder. *bioRxiv* (2021), p. 2021.10.12.464086.

719 76. J. Schindelin, I. Arganda-Carreras, E. Frise, V. Kaynig, M. Longair, T. Pietzsch, S. Preibisch, C.
720 Rueden, S. Saalfeld, B. Schmid, J.-Y. Tinevez, D. J. White, V. Hartenstein, K. Eliceiri, P.
721 Tomancak, A. Cardona, Fiji: an open-source platform for biological-image analysis. *Nat.*
722 *Methods.* **9**, 676–682 (2012).

724 **Acknowledgements:**

725 For the purpose of Open Access, the author has applied a CC BY public copyright licence to
726 any Author Accepted Manuscript version arising from this submission. We thank the
727 Newcastle University Flow Cytometry Core Facility; Sanger Institute Cellular Genetics IT;
728 Newcastle upon Tyne NHS Trust NovoPath; Tamilvendhan Dhanaseelan of HDBR for
729 assistance with human fetal tissue processing and cell freezing; Natalina Elliott for
730 contributions toward CITE-seq panel design.

731

732 **Funding:**

733 We acknowledge funding from the Wellcome Human Cell Atlas Strategic Science Support
734 (WT211276/Z/18/Z), MRC Human Cell Atlas award, Wellcome Human Developmental
735 Biology Initiative, and HDBR (MRC/Wellcome MR/R006237/1).

736 MH is funded by Wellcome (WT107931/Z/15/Z), The Lister Institute for Preventive Medicine
737 and NIHR and Newcastle Biomedical Research Centre.

738 SAT is funded by Wellcome (WT206194) and the ERC Consolidator Grant ThDEFINE.

739 Relevant research in the BG group was funded by Wellcome (206328/Z/17/Z) and the MRC
740 (MR/M008975/1 and MR/S036113/1).

741 IR is funded by Blood Cancer UK and by the NIHR Oxford Biomedical Centre Research Fund.

742 EL is funded by a Sir Henry Dale Fellowship jointly funded by the Wellcome Trust and the
743 Royal Society (107630/Z/15/A).

744 LJ is funded by an NIHR Academic Clinical Lectureship.

745 MMA is funded by an Action Medical Research Fellowship (GN2779).

746 NM was funded by a DFG Research Fellowship (ME 5209/1-1).

747 KG is funded by NIHR (MIC-2016-014).

748 SBe is funded by a Wellcome Senior Research Fellowship (10104/Z/15/Z).

749 CAI is funded by the Open Targets consortium (OTAR026 project) and Wellcome Sanger core
750 funding (WT206194).

751 MI is supported by the Wellcome Trust (215116/Z/18/Z) and thanks the PhD program FIRE
752 and the Graduate School EURIP of Université Paris Cité for their financial support.

753 JPal is funded by NIH NHLBI R01 (HL151777).

754

755 **Author contributions:**

756 Conceived and directed the study: MH, SAT, BG

757 Acquired HDBR fetal samples: SL, DH

758 Generated scRNA-seq datasets: JE, ES, IG

759 Generated CITE-seq datasets: ES, NKW, NM, RH, MSV

760 Performed light-sheet microscopy: YG, MI

761 Performed immunofluorescence: DD, MA

762 Performed immunohistochemistry: RC

763 Performed RNAscope: KK, LT

764 Performed mouse and human embryo imaging: SJK

765 Generated and interpreted iPSC data: CAI, RVT, VL

766 Performed CITE-seq data analysis and interpretation: AR, MQL, NKW

767 Performed scRNA-seq data analysis and interpretation: IG, SW, AR, KG, IIR, DMP, KP, JPar,

768 SvD

769 Interpreted the single cell data: OB, LJ, SBa, LG, MMA, KM, JPal, SBe, EL, AC, IR, MDB,
770 ED, CS

771 Wrangled the single cell data: SW, MMA, MQL, AR, NKW, IG

772 Led web portal development: DH, DBL

773 Prepared the manuscript: BO, MMi

774 Drafted the manuscript: LJ, SW, RB, IG, MH

775 Designed the manuscript figures: JE, RB, CAd

776

777 **Competing interests:**

778 All authors declare no competing interests.

779

780 **Data and materials availability:**

781 All novel raw sequencing data from this study are made publicly available at ArrayExpress as

782 FASTQs and count matrices as follows:

783 - i) Human embryonic liver and yolk sac 10x scRNA-seq (E-MTAB-10552)

784 - ii) Human embryonic yolk sac 10x scRNA-seq (E-MTAB-11673)

785 - iii) Human embryonic yolk sac Smart-seq2 scRNA-seq (E-MTAB-10888)

786 - iv) Human embryonic yolk sac CITE-seq (E-MTAB-11549)

787 - v) Human embryonic liver CITE-seq (E-MTAB-11618)

788 - vi) Human fetal liver CITE-seq (E-MTAB-11613)

789

790

791

792

793

794

795

796 Accessions for published data reused in this study are detailed comprehensively in **Table S6**.

797

798 Processed single cell datasets and supplementary tables are available for interactive
799 exploration and download as well as corresponding trained scVI and logistic regression
800 models via our interactive web portal (<https://developmental.cellatlas.io/yolk-sac>; password:
801 ys2022). Of note, data on portals are best used for rapid visualisation - for formal analysis it
802 is recommended to follow our GitHub code.

803

804 All code for reproducibility and trained logistic regression models of analysis is available at
805 https://github.com/haniffalab/FCA_yolkSac

806

807 **Supplementary Materials:**

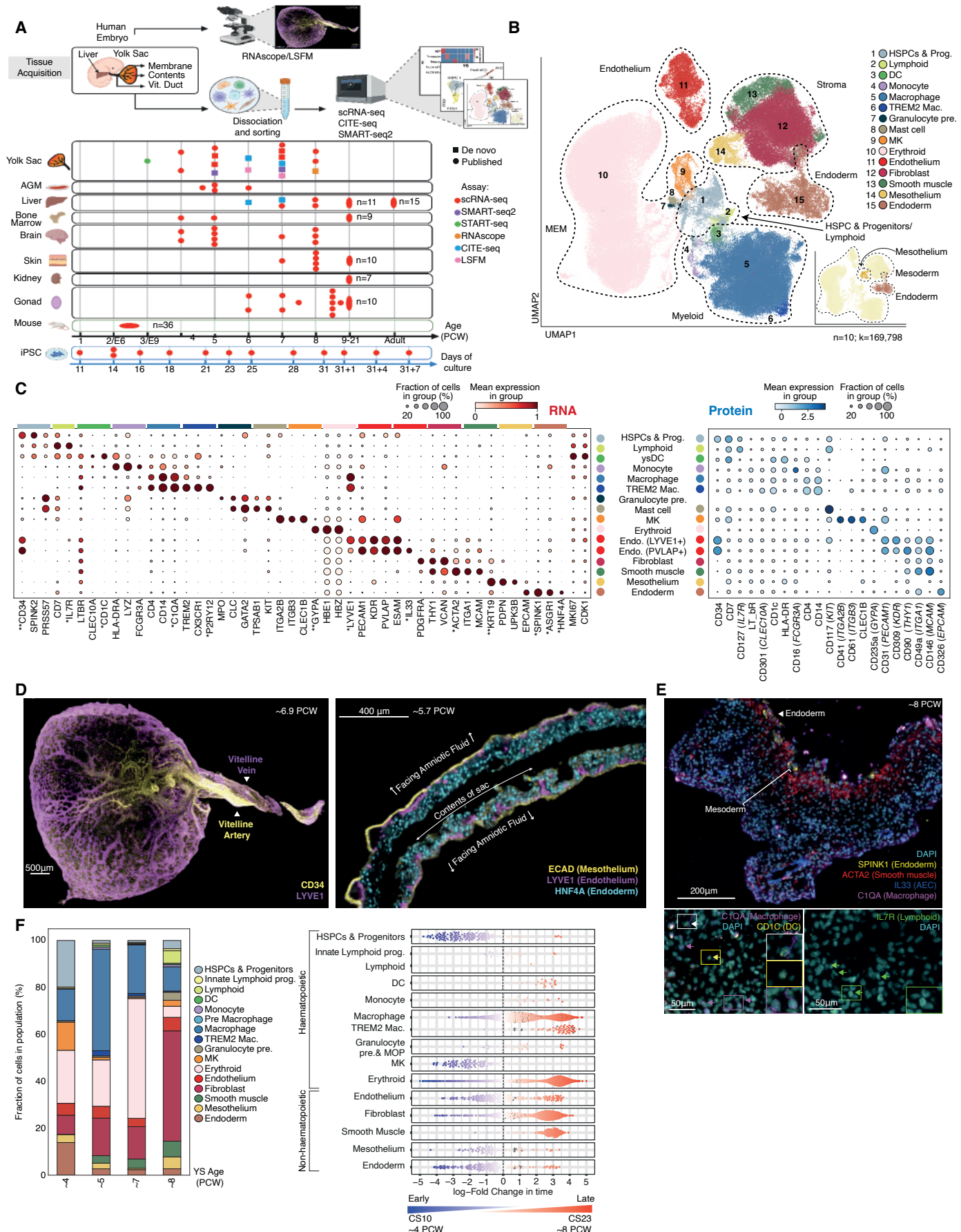
808 Materials and Methods

809 Figs S1 to S9

810 Refs 59 to 76

811 Tables S1 to S32

812 Movies S1 to S3



813 **Fig. 1: A single cell atlas of the human yolk sac**

814 (A) Summary of data included in analyses. Squares represent data generated for this study and
815 circles represent published datasets: YS (9, 11, 45, 53), AGM (11), liver (9), fetal BM (54),
816 fetal brain (44), fetal skin (45), fetal kidney (55), fetal gonads (46), mouse (56), iPSC (11, 21).
817 Shape colour indicates the assay used to generate data (**Table S6**).

818 (B) UMAP visualisation of YS scRNA-seq data (n=10 independent biological replicates;
819 k=169,798), with colours representing broad cell states: DC= dendritic cell, Mac= macrophage,
820 MEM= megakaryocyte-erythroid-mast cell lineage, MK= megakaryocyte, pre.= precursor.
821 Insert shows the same UMAP coloured by YS tissue layer (**Table S5**).

822 (C) Left: Dot plot showing the expression level (by colour) and percent expression (by dot
823 size) of broad cell state-defining genes in scRNA-seq data as shown in **b**, with data scaled to a
824 maximum value=1. Right: Dot plot showing equivalent protein expression (by colour) and
825 percent expression (by dot size) of broad cell states from n=2 biologically independent YS
826 CITE-seq samples, with data scaled zero_centre=False. * indicates genes validated by
827 RNAscope and ** indicates equivalent proteins validated by IHC/IF (**Table S4**).

828 (D) Light-sheet fluorescence microscopy images of YS. Left: CD34⁺ and LYVE1⁺ vascular
829 structures (representative ~6.9PCW sample; scale bar=500 μ m; **Movie S1-2**). Right: Location
830 of LYVE1⁺ vascular structures within HNF4A⁺ endoderm and adjacent to ECAD⁺
831 mesothelium (representative ~5.7PCW sample; scale bar=400 μ m).

832 (E) RNAscope images of YS, showing a representative 8PCW sample. Top: demonstrating
833 endoderm (*SPINK1*), smooth muscle (*ACTA2*), AEC (*IL33*) and macrophages (*C1QA*) (scale
834 bar=200 μ m). Bottom: demonstrating DCs (*CD1C*; yellow arrow), macrophages (*C1QA*;
835 magenta arrow), mac-DCs (*CD1C*⁺*C1QA*⁺; white arrow) and lymphoid cells (*IL7R*; green
836 arrow) (scale bar=50 μ m).

837 (F) Left: Bar graph showing the proportional representation of broad cell states to YS scRNA-

838 seq data grouped by gestational age in PCW. Right: Milo beeswarm plot showing differential
839 abundance of YS scRNA-seq neighbourhoods across time, where blue neighbourhoods are
840 significantly enriched (SpatialFDR<0.1,logFC<0) early in gestation (CS10-11), red
841 neighbourhoods are enriched later (CS22-23) (SpatialFDR<0.1,logFC>0) and colour intensity
842 denotes degree of significance. Abbreviations: as per (b) and MOP= monocyte progenitor and
843 pre= precursor (**Table S19**).

844

845

846

847

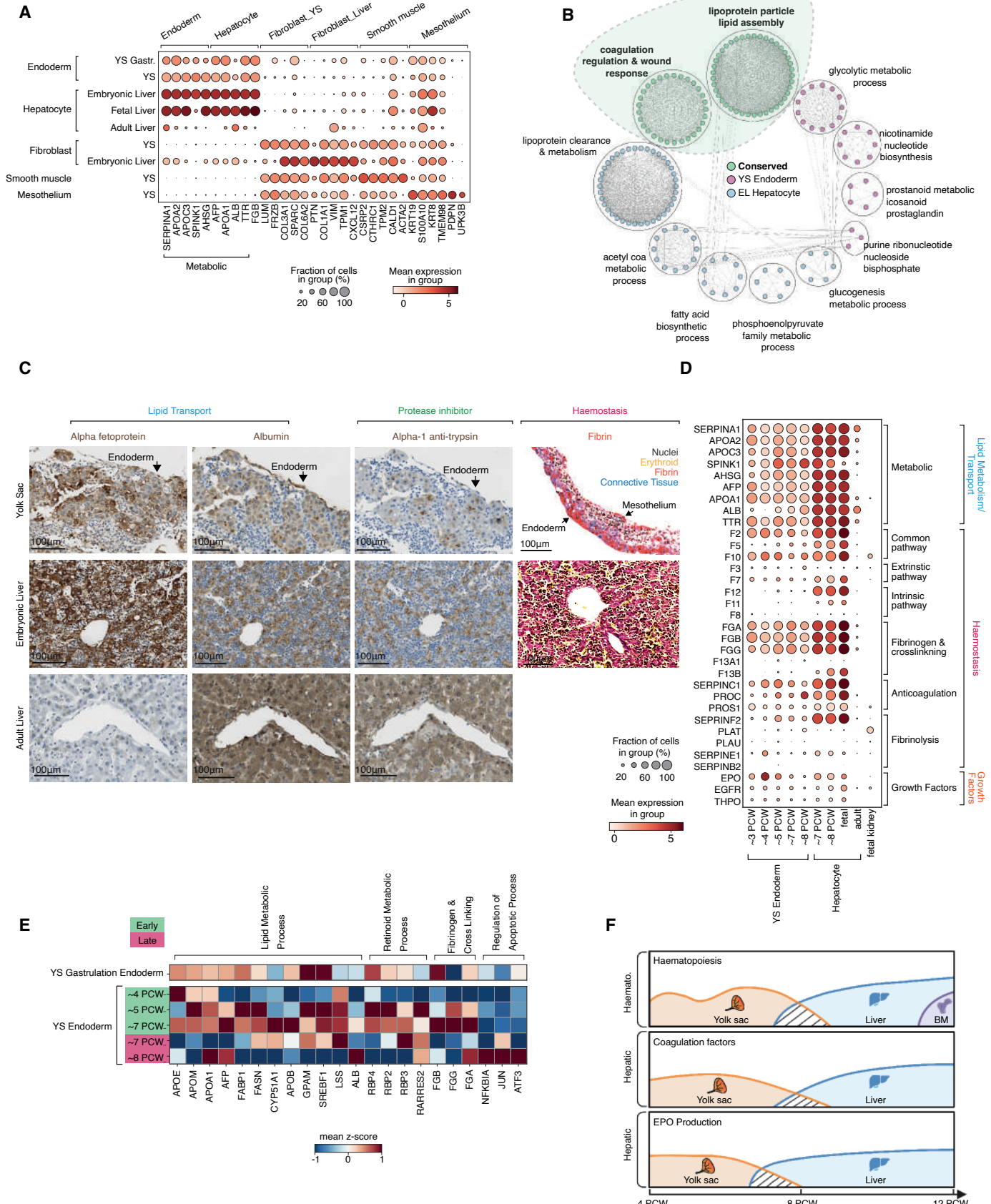
848

849

850

851

852



853 **Fig. 2: Multi-organ functions of YS**

854 **(A)** Dot plot showing the expression level (colour scale) and percent expression (dot size) of
855 DEGs in YS (main and gastrulation (gastr.) data) stromal cell states, matched embryonic, fetal
856 and adult liver stromal cell states and iPSC stromal cell states (21) (**Table S3, 20, 7**). All
857 datasets independently scaled to max value=10 and then combined, except YS and matched
858 EL scRNA-seq data which were scaled together. Genes involved in endoderm metabolic
859 function are grouped.

860 **(B)** Flower plot of the significant pathways upregulated in YS endoderm (pink), embryonic
861 liver (EL) hepatocytes (blue) and conserved across both tissues (green). Lines indicate
862 connected nodes of expression (**Table S21**).

863 **(C)** Left and middle: IHC staining of alpha fetoprotein (*AFP*), albumin (*ALB*) and alpha-1
864 antitrypsin (*SERPINA1*) in 8PCW YS, 8PCW EL and healthy adult liver. Representative
865 images from 1 of n=5 biological independent YS (4-8PCW), 1 of n=3 biologically independent
866 ELs (7-8PCW) and 1 of n=3 biologically independent adult livers. Scale bar=100 μ m. Right:
867 MSB-stained 8PCW EL (representative of n=3 biologically independent samples) and 4PCW
868 YS (representative of n=3 biologically independent samples). Nuclei (grey), erythroid
869 (yellow), fibrin (red), and connective tissue (blue). See ‘Immunohistochemistry’ section in
870 Methods for details regarding pseudo-colouring shown. Scale bars=100um.

871 **(D)** Dot plot showing the expression level (colour scale) and percent expression (dot size) of
872 haemostasis factors expressed by YS endoderm (main and gastrula data), embryonic, fetal and
873 adult liver hepatocytes, and endoderm from fetal kidney (55). Grouped by pathway and role.
874 All datasets independently scaled to max value=10 and then combined, except YS and matched
875 EL scRNA-seq data which were scaled together.

876 (E) Matrix heatmap of Milo-generated DEGs in endoderm from YS scRNA-seq including
877 gastrulation datasets (**Table S19**). DEGs are grouped by function. Each dataset scaled zero
878 centre=False and YS endoderm standard_scale='var'.

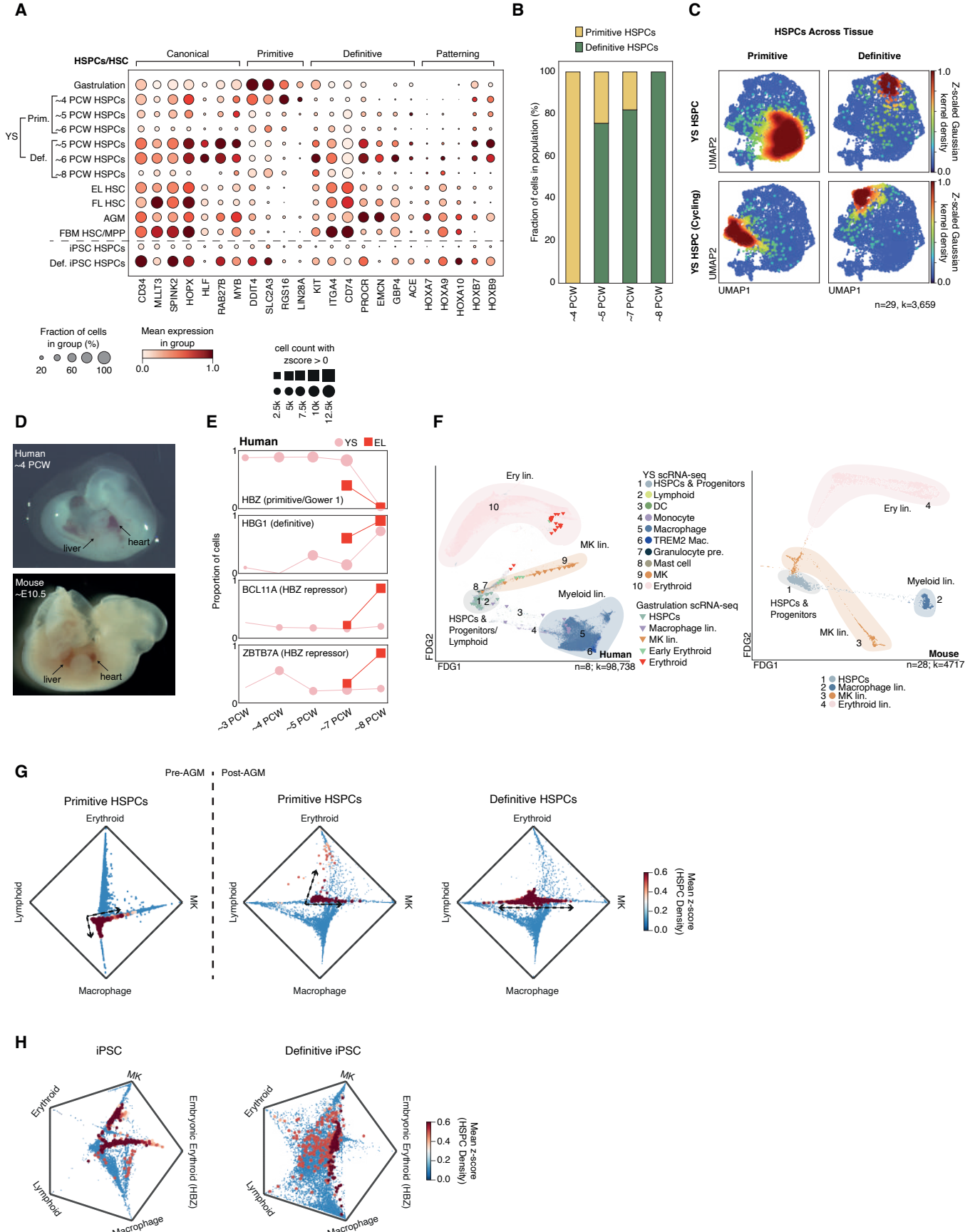
879 (F) Schematic of the relative contribution of YS (orange), EL (blue), BM (purple) to
880 haematopoiesis, coagulation factors and EPO synthesis in the first trimester of human
881 development.

882

883

884

885



886 **Fig. 3: Primitive versus definitive haematopoiesis in YS and liver**

887 **(A)** Dot plot showing the mean variance scaled expression level (colour scale) and percent
888 expression (dot size) of canonical, primitive and definitive, and patterning HSC markers
889 expressed between YS HSPCs, including gastrulation (57), AGM HSPC (58), matched EL
890 HSC, FL HSC (9), fetal BM HSC/MPP (54), iPSC-derived HSPC (21) and definitive iPSC-
891 derived HSPC (11).

892 **(B)** Bar graph showing the proportional representation of primitive YS HSPCs to definitive YS
893 HSPCs in the main YS scRNA-seq data (grouped by gestational age in PCW).

894 **(C)** Density plots showing the distribution of YS HSPC (top), cycling HSPC (bottom) with
895 primitive (left) and definitive signatures (right) in the integrated UMAP landscape of
896 HSPC/HSCs from YS including gastrulation (n=10, k=2,597), AGM (58) (n=1, k=28),
897 matched embryonic liver (EL) (n=3, k=412), fetal liver (FL) (9), fetal bone marrow (54) (FBM)
898 (n=9, k=92), iPSC-derived HSPC (21) and definitive iPSC-derived HSPC (11) scRNA-seq
899 datasets. Colour of HSC/HSPC cells represents the z-scored kernel density estimation (KDE)
900 score for each population (**Table S5**).

901 **(D)** Image of a ~4PCW/CS12 human embryo (top; representative from n=4 biologically
902 independent samples) and ~E10.5/CS12 mouse embryo (bottom; n=1) with the heart and liver
903 labelled.

904 **(E)** Line graphs showing the relative change in proportion of erythroid lineage cells (y-axis)
905 enriched in expression of globins over gestational age, including *HBZ*, *HBG1* and HBZ-
906 repressors *BCL11A* and *ZBTB7A*. Pink lines= human YS main and gastrulation scRNA-seq
907 data. Red lines= matched scRNA-seq data. Globins are grouped by their role in primitive
908 haematopoiesis, definitive haematopoiesis and repression.

909 **(F)** Force directed graph (FDG) visualisation of haematopoietic cell states in the YS scRNA-
910 seq dataset (n=8, k=98,738; dots) integrated with human gastrulation (57) scRNA-seq dataset

911 (n=1, k=91; triangles) (left), and equivalent cell states found in the mouse gastrulation scRNA-
912 seq dataset (56) (n=28, k=4,717; dots) (right). Colours represent cell states and clouds mark
913 lineages

914 **(G)** Circular plots showing relative absorption probabilities of lineage-state transition between
915 primitive HSPCs in the YS pre-AGM (CS10-11) (left) and primitive and definitive HSPCs in
916 the YS post-AGM (>CS14) (right). Colour indicates the HSPC population density as a z-scored
917 kernel density estimation (KDE) score and the position of HSPC population densities indicate
918 respective lineage priming probability between Macrophage, lymphoid (NK and B lineage),
919 erythroid and MK terminal states.

920 **(H)** Circular plots showing relative absorption probabilities of lineage-state transition between
921 iPSC-derived HSPCs (left) and definitive iPSC-derived HSPCs (right). Colour indicates the
922 HSPC population density as a z-scored kernel density estimation (KDE) score and the position
923 of HSPC population densities indicate respective lineage priming probability between
924 Macrophage, lymphoid (NK and B lineage), erythroid (any erythroid cell with individual Z-
925 score of HBA1,HBA2,HBG1,HBG2,HBD > 0), embryonic erythroid (any erythroid cell with
926 HBZ Z-score > 0) and MK terminal states.

927

928

929

930

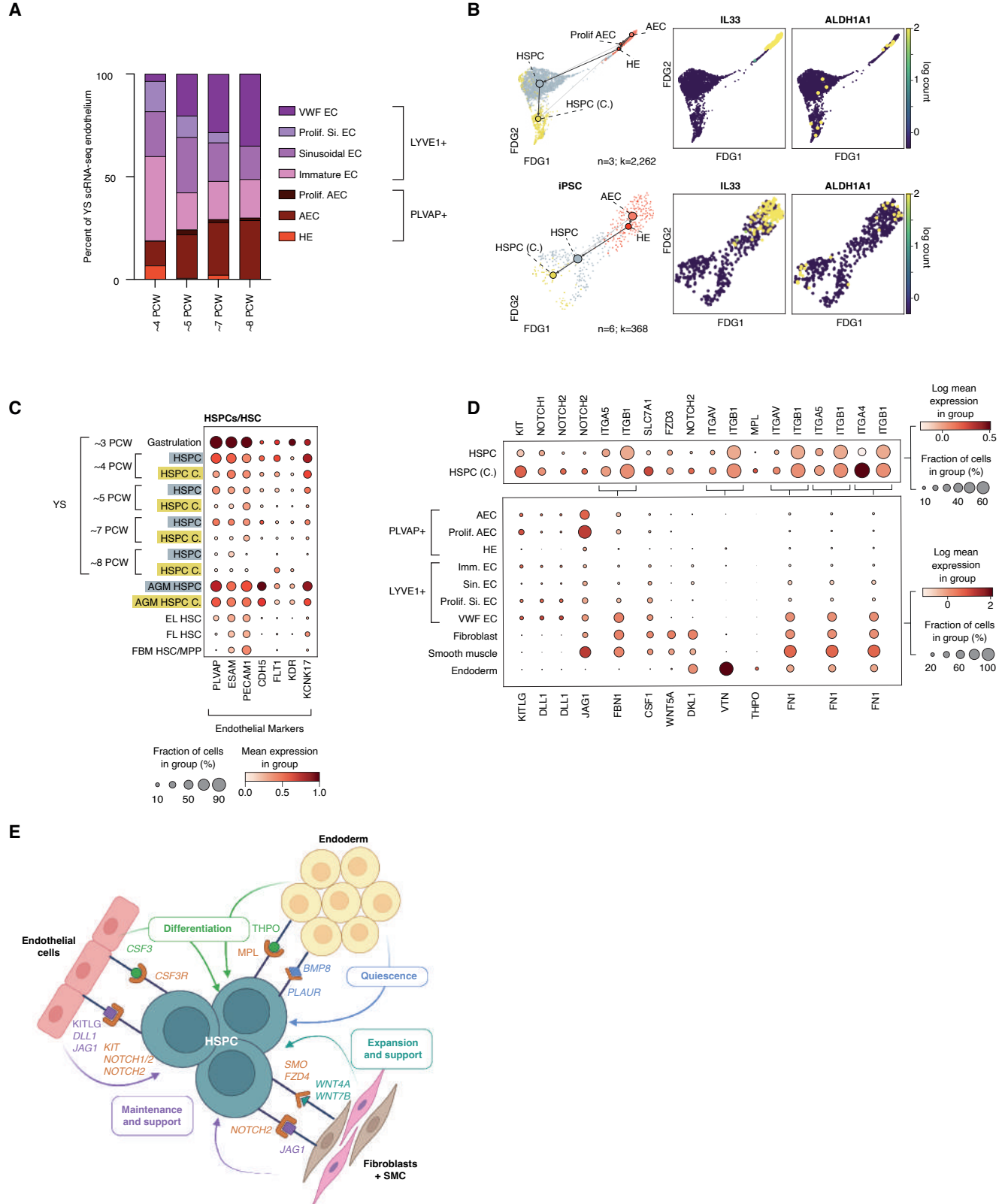
931

932

933

934

935



936 **Fig. 4: The lifespan of YS HSPCs**

937 **(A)** Barplot showing the relative proportion of YS endothelial cell subsets grouped by PCW.

938 **(B)** FDG overlaid with PAGA showing trajectory of HE transition to HSPC in YS scRNA-seq
939 data (n=3; CS10, 11 and 14; k=2,262) (top) and iPSC-derived HSPC scRNA-seq data (n=7,
940 k=437) (21) (bottom), with feature plots of key genes (*IL33*, *ALDH1A1*) involved in endothelial
941 to hemogenic transition (**Table S5**).

942 **(C)** Dot plot showing the expression level (colour scale) and percent expression (dot size) of
943 genes associated with endothelial cells in HSPCs from YS (including gastrulation) scRNA-seq,

944 AGM (11), matched EL (embryonic liver), FL (fetal liver) (9) and fetal bone marrow BM (32).

945 **(D)** Heatmap showing relative mean expression z-scores of curated and statistically significant
946 (p<0.05) CellphoneDB putative receptor ligand interactions between YS endothelial subsets vs
947 HSPC across gestation. Growth factor, TGF beta and NOTCH ligand receptor -related gene
948 interactions have been highlighted.

949 **(E)** Schematic of selected and statistically significant (p<0.05) CellphoneDB putative receptor
950 ligand interactions between YS HSPC vs endoderm, fibroblasts (Fib), smooth muscle cells
951 (SMC) and endothelial cells (EC) in scRNA-seq data. Receptors and ligands in italics
952 significantly decrease CS17-12 (6-8PCW). See CellPhoneDB methods and **Table S23-24**.

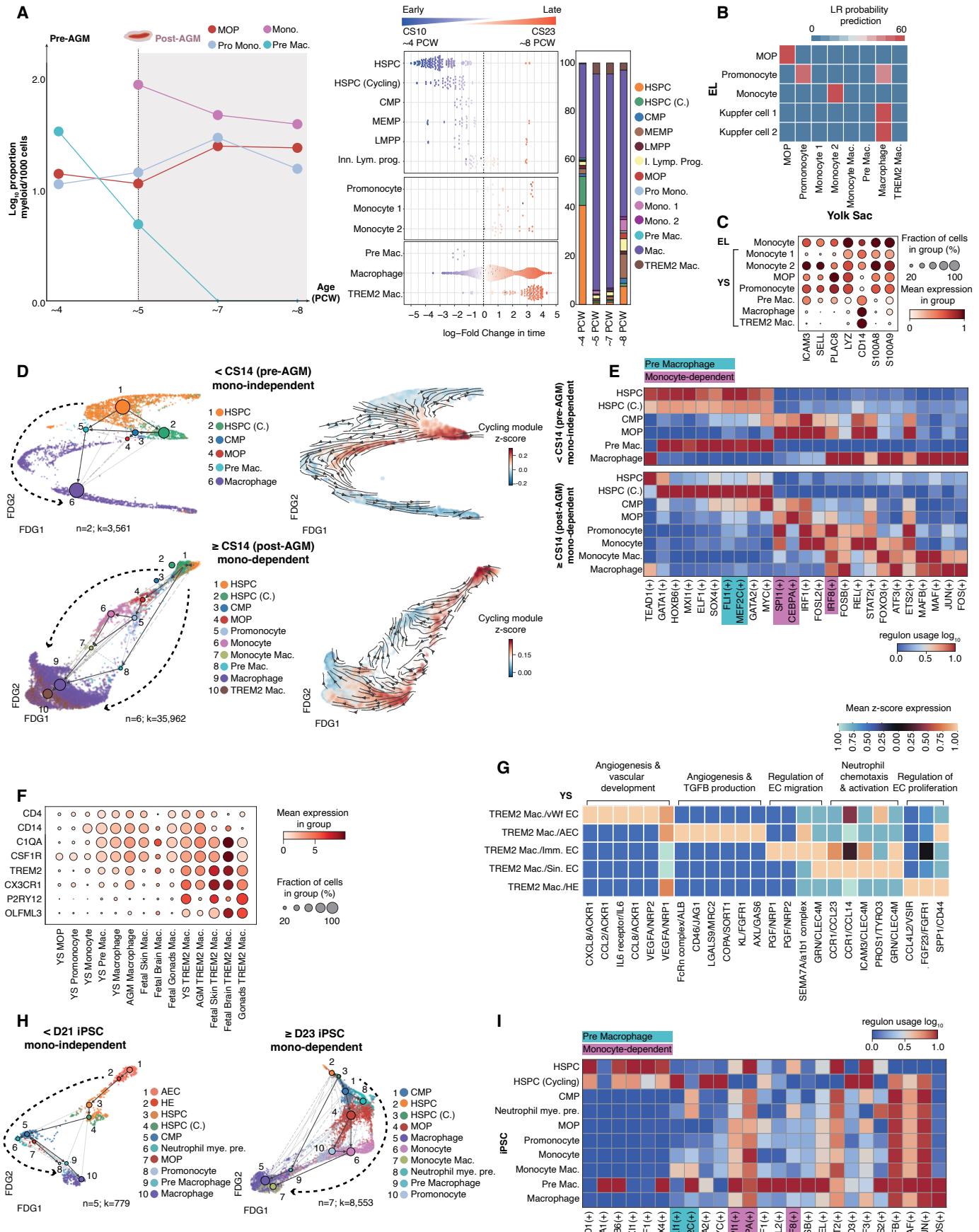
953

954

955

956

957



958 **Fig. 5: Accelerated macrophage production in YS and iPSC culture**

959 **(A)** Left: Line graph showing the proportion of monocyte progenitors (MOP), promonocytes
960 (pro mono), monocytes (mono) and pre macrophage (pre mac) in yolk sac (YS) over gestational
961 age. Dashed line indicates the stage before (left) and after (right) AGM involvement. Middle:
962 Milo beeswarm plot showing differential abundance of YS scRNA-seq myeloid
963 neighbourhoods across time, where blue neighbourhoods are significantly enriched
964 (SpatialFDR<0.1,logFC<0) early in gestation (CS10), red neighbourhoods are enriched later
965 (CS23) (SpatialFDR<0.1,logFC>0) and colour intensity denotes degree of significance.
966 HSPC= haematopoietic stem and progenitor cells, CMP= common myeloid progenitors,
967 MEMP= mast, erythroid and megakaryocyte progenitors, LMPP= lymphoid-primed
968 multipotent progenitors, inn. lymph. prog.= innate lymphoid progenitor, MOP= monocyte
969 progenitor, mono= monocyte, mac=macrophage Prog.= progenitor, pre=, precursor, MK=
970 megakaryocyte (**Table S19, 4**). Right: Bar graph showing the proportional representation of
971 myeloid cell states in YS scRNA-seq data grouped by gestational age in PCW.
972 **(B)** Median logistic regression class prediction probabilities for a model trained on YS scRNA-
973 seq myeloid cell states (x-axis) projected onto equivalent cell states in matched embryonic liver
974 (EL) scRNA-seq (y-axis)(**Table S12**).
975 **(C)** Dot plot showing the expression level (colour scale) and percent expression (dot size) of
976 DEGs and known monocyte markers in YS myeloid cell states shown in **b** compared to
977 matched EL monocytes (standard_scale='var') (**Table S28**).
978 **(D)** Left: FDG overlaid with PAGA showing monocyte-independent trajectory from YS
979 scRNA-seq HSPC to macrophage prior to CS14 (pre-AGM; n=2; k=3,561; top) and monocyte-
980 dependent trajectory to macrophage after CS14 (post-AGM; n=6; k=35,962; bottom). Left:
981 Coloured by cell state. HSPC, haematopoietic stem cell; CMP, common myeloid progenitor;
982 MOP, monocyte progenitor (**Table S5**). Right: CellRank state transition matrix inferred arrows

983 projected onto FDG indicate the trend of trajectory, and colour shows z-score enrichment in
984 cycling module (GO:0007049) genes.

985 (E) Matrix heatmap showing the pySCENIC-derived regulons associated with the YS
986 macrophage trajectories as shown in **d** for monocyte-independent, and monocyte-independent
987 routes of differentiation.

988 (F) Dot plot showing the level (colour scale) and percent expression (dot size) of macrophage
989 and microglia markers within the YS scRNA-seq monocyte and macrophage lineage in
990 comparison to microglia, microglia-like and macrophage cell states in AGM (*11*), fetal skin
991 (*45*), fetal gonads (*46*) and fetal brain (*44*). Fetal brain, skin and gonad cell states annotated in-
992 house using LR output provided in **Fig. S8E**. Each dataset was scaled independently to a
993 max_value = 10 then combined for plotting (**Table S18**).

994 nocyte-dependent trajectories in the YS scRNA-seq dataset (including gastrulation).

995 (G) Heatmap visualisation of CellphoneDB predicted interactions between TREM2⁺
996 microglia-like and endothelial cell states in the YS scRNA-seq (**Table S23**). Colour scale
997 represents z-scored mean expression values of each gene pair.

998 (H) FDG overlaid with PAGA showing monocyte-independent trajectory from iPSC scRNA-
999 seq (*21*) AEC to macrophage prior to D21 (n=5; k=779; left) and monocyte-dependent
1000 trajectory to macrophage after D21 (n=7; k=8,553; right). Arrows indicate the trend of
1001 trajectory. Coloured by cell state (**Table S7, S5**).

1002 (I) Matrix heatmap showing the pySCENIC-derived regulons associated with the iPSC
1003 macrophage trajectories as shown in **i** for the iPSC scRNA-seq dataset (*21*).

1004

1005

1006

1007